NACA TN 4151 10488

TECH LIBRARY KAFB, NM
0067038

NATIONAL ADVISORY COMMITTEE FOR AERONAUTICS

TECHNICAL NOTE 4151

CORRELATIONS AMONG ICE MEASUREMENTS, IMPINGEMENT RATES ICING CONDITIONS, AND DRAG COEFFICIENTS FOR UNSWEPT NACA 65A004 AIRFOIL

By Vernon H. Gray

Lewis Flight Propulsion Laboratory
Cleveland, Ohio

Washington
February 1958

AFMDC
TECHNICAL LIBRARY

TECH LIBRARY KAFB, NM

0067038

4438

CC-1

NATIONAL ADVISORY COMMITTEE FOR AERONAUTICS

TECHNICAL NOTE 4151

CORRELATIONS AMONG ICE MEASUREMENTS, IMPINGEMENT RATES, ICING CONDITIONS, AND DRAG COEFFICIENTS FOR UNSWEPT NACA 65A004 AIRFOIL

By Vernon H. Gray

SUMMARY

An empirical relation has been obtained by which the change in drag coefficient caused by ice formations on an unswept NACA 65A004 airfoil section can be determined from the following icing and operating conditions: icing time, airspeed, air total temperature, liquid-water content, cloud droplet impingement efficiencies, airfoil chord length, and angles of attack. The correlation was obtained by use of measured ice heights and ice angles. These measurements were obtained from a variety of ice formations, which were carefully photographed, cross-sectioned, and weighed. Ice weights increased at a constant rate with icing time in a rime icing condition and at progressively increasing rates in glaze icing conditions. Initial rates of ice collection agreed reasonably well with values predicted from droplet impingement data. Experimental droplet impingement rates obtained on this airfoil section agreed with previous theoretical calculations for angles of attack of 4° or less. Disagreement at higher angles of attack was attributed to flow separation from the upper surface of the experimental airfoil model.

INTRODUCTION

Over the last several years considerable information about aircraft icing characteristics and the resultant aerodynamic penalties has been acquired. This information now generally permits: (1) calculation of cloud droplet impingement rates for a variety of body shapes and flight conditions, (2) prediction of the area of a body on which ice formations will occur and the general nature of the ice (rime or glaze), and (3) for several airfoils, estimation of aerodynamic penalties due to ice formations acquired during exposure to a variety of specified icing conditions. Unfortunately, very little direct correlation has been shown among these three facets of the icing problem. The impingement calculations do not quantitatively foretell size, shape, or even weight of ice

that will form under given conditions, nor are the published aerodynamic penalties related to the actual ice size and shape, except in a gross way. Furthermore, it is difficult to estimate aerodynamic penalties in icing conditions different from those specifically investigated for a particular airfoil.

In analyses of data from previous icing studies several possible relations or trends have become evident, although exact measurements are lacking. One of these trends concerns the impingement rate on a body as it steadily collects ice. Past evidence has shown that in some cases the ice growth is sufficient to change the body shape and thereby affect the impingement rate as the ice grows in size. Another relation is indicated between the ice shape and the conditions under which the ice is formed (such as air temperature, airspeed, liquid-water content, etc.). Such a relation is discussed in reference 1, in which the class of ice (mushroom, intermediate, or streamlined) is predictable by calculations. Also, studies of aerodynamic penalties associated with ice formations and flow spoilers on airfoils indicate that a direct relation should exist between ice shape and size and the changes in aerodynamic characteristics caused by the ice.

Because of the limitations in current analytical treatments of aerodynamic data for icing conditions, and because previous aerodynamic studies in icing conditions have indicated the key importance of ice shape, the present investigation was undertaken to measure ice formations, impingement rates, and aerodynamic characteristics associated with icing of an unswept NACA 65A004 airfoil section and to determine the interrelations between these quantities and the imposed icing and operating conditions. Changes in aerodynamic coefficients (lift, drag, and pitching moment) caused by ice formations on this 4-percent-thick airfoil section are presented in reference 2, and pertinent values of these drag coefficients and associated data are summarized in the present report for use in developing the correlations. This report may be considered a companion to and an extension of reference 2. This investigation was conducted in the NACA Lewis 6- by 9-foot icing tunnel over a wide range of icing conditions at airspeeds up to 275 miles per hour (240 knots) and geometric angles of attack up to 11°.

APPARATUS AND PROCEDURE

The model used in this study was an unswept NACA 65A004 airfoil section of 6-foot chord and 6-foot span mounted vertically in the Lewis icing tunnel (fig. 1). The model was steam heated to prevent tunnel frost deposits, except for a leading-edge section of 42-inch span and approximately 19-inch chord (27 percent of maximum chord). This icing test section was built of wood and covered with a neoprene sheet 0.010 inch thick to resist abrasion.

The equipment and procedures used to obtain aerodynamic forces on the clean and iced airfoil model are discussed in reference 2. The aerodynamic measurements cited in the present report are not corrected for tunnel wall effects. The angles of attack quoted are the geometric angles between the airfoil chord line and the tunnel centerline. Because the airfoil section was symmetrical, only positive angles of attack were considered in this investigation.

Icing conditions in the tunnel were obtained and measured according to previously established techniques and calibrations. The factors that constitute an icing condition were varied independently over their available ranges with one exception: the cloud droplet sizes increased with increases in the liquid-water content and decreases in velocity because of limitations in the design of the tunnel spray system.

Generally, an icing run consisted of a 3- to 18-minute exposure of the airfoil to a particular set of constant icing conditions during which the aerodynamic forces on the model were recorded and after which the tunnel was stopped and entered to obtain measurements of the final ice formation on the unheated leading-edge section. After some of the runs, the airfoil with ice acquired during the run was turned to various angles of attack, and the aerodynamic forces at each angle were recorded in clear air (no icing sprays).

4438

CC-1 back

Ice Measurement Techniques

Two principal operations were performed to obtain the desired ice measurements; a representative sample of the ice was weighed, and a typical chordwise cross section of the ice was photographed. To accomplish the first objective, a thin sheet of celluloid about 4 inches wide was taped around the clean-airfoil leading edge near midspan and extended chordwise to the rear of the leading-edge section, as shown in figure 2(a). The tunnel was then started, and a particular icing condition was established. After an icing period, the airfoil ice deposit appeared, for example, as shown in figures 2(b) and (c). The observed ice formations were all quite uniform along the span, and the celluloid strip had a negligible effect on the local ice accretion or shedding tendencies.

To obtain the weight of ice that formed on the celluloid, the tunnel was stopped and maintained below freezing while the ice that covered the edge tapes was removed by a steam-heated ice scraper as shown in figure 2(d). This scraper also had an internal vacuum chamber that sucked in the water through several small holes as rapidly as the ice was melted. In this way water was prevented from running into the ice sample and affecting its weight or shape. Below the celluloid strip enough ice was removed to permit insertion of a metal catch pan formed to fit around the clean airfoil (fig. 2(d)). Then the tapes were removed, and the

celluloid strip with its ice sample was loosened from the airfoil and placed in the pan along with any stray ice particles that might have broken loose. By weighing the pan and contents and subtracting the dry tare weight, the weight of ice collected over 4 inches of span was obtained.

After removal of the celluloid and the ice sample and pan, the ice on the airfoil for about 18 inches above the pan position was removed with the ice scraper in preparation for photography. The edge of the ice formation upon which the pan had been resting was then dressed into a plane surface perpendicular to the leading edge. A 1/4-inch mesh wire grid, painted black, was then placed upon the ice in a manner similar to that for the pan (see fig. 2(e)). Below the wire screen (about 2 in.) a slit in the ice was cut with the scraper in order to allow insertion of a black cardboard for contrasting background. The camera was then positioned above the wire screen near the airfoil leading edge and directed nearly vertically downward. A resulting photograph is shown in figure 2(f). The white wire of the screen (fig. 2(f)) was alined to be an extension of the airfoil chordline. By using the 1/4-inch spacing of the grid and a point-plotting procedure which took the camera angle into account, full-scale two-dimensional cross sections of the various ice formations were then made and reduced to convenient size for study and illustration (inset on fig. 2(f)). Generally, two or three photographs were made after each icing run with slightly different angles, positions, and lighting conditions to reduce the errors due to perspective.

4438

Impingement Tests

Water-droplet impingement data were obtained for the 6-foot-chord airfoil model shown in figure 1. To increase the range of the impingement parameters, impingement data were also obtained for a 13-inch-chord (6-foot-span) wooden airfoil of the same section (NACA 65A004). To obtain the rates of droplet impingement upon the airfoils, dye was added to the tunnel spray water, and absorbent blotter strips were secured to the airfoil surface. The amount of dye contained in the water droplets that impinged on the blotter strips was determined by colorimetric analysis of samples punched out of the blotters. In this way, impingement rates on the airfoil could be calculated for both local and total values. The detailed procedure for obtaining impingement values with this dye-tracer technique is given in reference 3, and the analysis of colorimetric data as applied to airfoils is described in reference 4.

RESULTS AND ANALYSIS

Impingement Data

The distribution of local droplet impingement over the surface of the 6-foot-chord airfoil is shown in figure 3 in nondimensional form. The local impingement values are presented in terms of the local impingement efficiency $\overline{\beta}$, which is the ratio of the local impingement rate $\overline{W}_\beta$ (lb water/(hr)(sq ft)) to the product $0.329\ V_0 w$, plotted against dimensionless chordwise surface distance s/c for four angles of attack. (Symbols are defined in the appendix.) Generally, the trends in figure 3 are similar to those in the data for thin airfoils previously published (refs. 4 to 7). The impingement pattern at zero angle of attack (fig. 3(a)) is essentially symmetrical with respect to the upper and lower surfaces of the airfoil. The value of $\overline{\beta}$ at the leading edge has a maximum of 0.79 and falls off rapidly on either side of the leading edge. For the cloud conditions studied, practically all of the impingement at zero angle of attack occurred over the first 2 percent of chord. However, at angles of attack of 2° and higher, impingement terminates close to the leading edge on the upper surface (within 1 percent of chord) and extends a considerable distance downstream on the lower surface (to near the point of maximum thickness with large drop sizes)[1] (figs. 3(b) to (d)). Beyond about 20 percent chord, however, impingement on the lower surface is at a very low rate ($\overline{\beta} < 0.015$ for the conditions investigated). Because of their greater inertia, the larger drops generally produced the higher local impingement efficiencies.

The total droplet impingement efficiency for the airfoil $\overline{E}_m$ is obtained from the area under the $\overline{\beta}$ curves in figure 3 and is defined as $(c/H)\int\overline{\beta}\ d(s/c)$ between the limits of impingement on upper and lower surfaces. In this definition, $\overline{E}_m$ is based on the projected frontal height of the airfoil H, values of which can be obtained from table I. For interpolation purposes it is convenient to present $\overline{E}_m$ and other impingement variables in terms of a modified inertia parameter K_0. This parameter is completely described and defined in reference 3. An approximation of K_0 that is within ± 5 percent error over the usual range of impingement calculations (free-stream Reynolds number between 25 and 1000, based on volume-median droplet diameter) is obtained from

[1]Impingement limits are taken as the points where the $\overline{\beta}$ values first reach a constant minimum level. The minimum levels vary slightly from case to case depending on tunnel humidity, dirt content, etc.

the expression $K_0 \approx 1.87\times10^{-7}\left(\frac{V_0}{\mu}\right)^{0.6} \frac{d^{1.6}}{\rho^{0.4}c}$. The experimental impingement efficiency $\overline{E}_m$ obtained in the present investigation with both the 6-foot- and 13-inch-chord airfoils is plotted against K_0 in figure 4 and compared with theoretical values from references 5 to 7. The theoretical values of impingement efficiency $\overline{E}_m$ were calculated using a weighted distribution of droplet sizes according to a Langmuir "D" distribution (nearest to tunnel distribution) and were found to be practically equal to the impingement-efficiency values for the volume-median droplet sizes. The values of $\overline{E}_m$ increase with increasing K_0 and reach a maximum (experimental) value of 0.49 at an angle of attack of 4° ($K_0 = 0.092$). Similar plots against K_0 can be made for various $\overline{\beta}$ values at constant s/c locations and for the maximum values ($\overline{\beta}_m$).

The agreement between experimental and theoretical impingement at 0° and 4° angles of attack was good. However, a sizable discrepancy between theory and experiment occurred at the 8° angle of attack, where the experimental $\overline{E}_m$ values were only about half the theoretical values. This disagreement can be largely reconciled by the following study of the flow fields involved.

The local velocity distribution over the airfoil used in the present experimental tests at 0°, 4°, and 8° angles of attack is compared in figure 5 with the velocity distribution assumed in the theoretical impingement calculations of references 5, 6, and 7, respectively. At 0° and 4° angles of attack the local velocity ratios agree quite well, with a slight tendency toward higher velocities in the experimental case. However, at an 8° angle of attack, the experimental velocity distribution differs markedly from the theoretical. The experimental stagnation point is farther forward, the lower-surface and trailing-edge velocities are greater, and the upper-surface velocities peak lower and describe a region of approximately constant velocity just aft of the peak. All of these deviations indicate that flow separation occurs on the upper surface, a common condition with thin, symmetrical, sharp-nosed airfoils. Experimental evidence of the effect of flow separation on impingement is not available, but an analogous condition has been investigated. In a study of the effect on impingement of truncating an airfoil (ref. 8), the velocity distributions over the airfoil forward regions at angles of attack were affected in a manner very similar to that herein caused by flow separation. The effect of such truncating was to reduce the airfoil impingement rate substantially. Therefore, flow separation would also be expected to reduce the experimental impingement rates below the theoretical.

Comparison of Weight of Ice Collected with Impingement Calculations

Several icing runs were made to compare the weight of ice collected on the airfoil with the weight predicted by impingement calculations. To determine whether the ice collection rates varied with icing time, the runs were repeated for varying lengths of time in identical icing conditions. After each run, the ice collections were weighed and photographed. The results of these tests are listed in table II and plotted in figure 6.

4438

The weight of ice collected in some of the conditions increased faster than a linear rate with icing time (fig. 6). These conditions were such as to produce glaze icing deposits. (An empirical means of determining the glaze or rime characteristic of icing is presented in a later section.) One such glaze icing condition is illustrated in figure 6 with ice cross sections at 3, 6, and 10 minutes of icing time. The ice growth obviously changes the airfoil characteristics and causes a continual increase in the collection rate above the initial rate (initial rate of 0.07 lb/(min)(ft span) compared with 0.25 lb/(min)(ft span) after 10 min). The ice formation shown after 10 minutes of glaze icing is nearly as large (normal to the chord line) as the maximum airfoil thickness, which is shown by the vertical line on the right of the sketch. The ice cross sections for the other data points of figure 6 are given in table II. The set of points for the 0° F air total temperature describe a linear curve with icing time, and the corresponding ice formations are of the rime type, which tends to build forward in the direction of the local airstream. A rime ice formation generally causes little change in airfoil shape, and in the example at 0° F, has no effect on the ice collection rate.

Inasmuch as the ice collection rate increases with icing time for many of the conditions investigated, a meaningful comparison with the water impingement rate $\overline{W}_m$ (predicted from the experimental data of figure 4) can be made only with the initial ice collection rate (unchanged airfoil shape). The initial ice collection rates listed in figure 6 are obtained from the slopes of the faired curves at the origin. The ratios of these collection rates to the rates predicted from the experimental impingement data of figure 4 are given for the six examples and vary from 0.80 to 1.33, the average value being about 1.06. Considering the nature and difficulties of making both ice and impingement measurements, this order of agreement appears quite satisfactory.

Ice Shape Factors

Data presented in the preceding section are helpful in determining the weight of ice on an airfoil by calculation means from known impingement relations. However, as previously stated, the aerodynamic effects

of ice formations appear to be functions of their size, shape, and location on the airfoil. For example, as shown in reference 9, changes in airfoil-section drag coefficients due to ice formations can be grossly explained in terms of drag changes due to variously shaped airfoil spoilers and protuberances, data for which are given in reference 10. Data of reference 11 further demonstrate that drag coefficients often vary almost linearly with spoiler height, and that spoiler (and ice) chordwise location is very critical in the leading-edge region. For these reasons, the present correlation between ice formations and aerodynamic drag was attempted by using height and angle measurements of the ice deposits rather than their weights.

The ice deposits in the present study are represented by two dimensions, h and θ, as shown in figure 7. Dimension h is the height of the edge of the ice first reached in going from the upper to the lower surface. The angle θ is measured between this ice edge and the extended chord line. The angle is positive if above the chord line and negative if the ice edge falls below the extended chord line. These measurements are given in table II for most of the icing runs.

Representation of ice formations by these two dimensions only ignores the part of the ice toward and on the lower surface of the airfoil. Generally, protuberances on this region contribute very little drag to the airfoil, except near zero angle of attack. In contrast, flow spoilers near the leading edge and toward the upper surface cause large drag increases; this surfacewise variation in effect of spoilers is illustrated in reference 11 and is directly related to the local-velocity distribution over the airfoil. On the present 65A004 airfoil section the ice formations on the upper surface extended only a very short distance from the zero-chord point, as indicated in table II. Consequently, for this airfoil section, little variation in chordwise location of the significant ice deposit occurred, and chordwise measurements of ice deposits were abandoned in favor of the ice angle θ. This angle, in conjunction with h, thus determines the critical feature of an ice deposit with respect to aerodynamic drag; also, θ provides a scale of measurement of the type of ice (from rime to glaze).

Correlation Between Ice Shape and Icing Conditions

Ice angle. - In the data of table II, the ice angle θ increases with increasing impingement rates and air temperatures and decreasing angles of attack. An empirical relation between these variables is shown in figure 8 for the present airfoil data. The ice angle θ in the abscissa of figure 8 is modified by the addition of the expression $58\left(1 - \frac{1}{1.35^{\alpha_i}}\right)$ to account for the variation of θ with the angle of attack α_i.

The abscissa is thus a measurement of the type of ice formation, with a value of 32 approximately dividing the observed rime ice from the glaze ice. The ordinate of figure 8 is the expression $w^{1/2}\left(\frac{\overline{E}_m}{32 - t_0}\right)^{1/3}$. Although considerable scatter of data points exists, the exponents and coefficients were each adjusted until an equal scattering of data about an average straight line was obtained.

For the present data, air velocity had a negligible effect on θ, and the best correlation was obtained with the velocity term absent. As mentioned previously, the tunnel-cloud droplet size varied according to the liquid-water content and velocity, and thus the effect on ice angle of the droplet size as an independent variable was not obtainable. However, the $\overline{E}_m$ factor in the ordinate is sensitive to changes in drop size, and the present conclusion is in substantial agreement with unpublished NACA flight data obtained for various ice formations on a 1/2-inch-diameter cylinder.

The expression resulting from the plot in figure 8 is as follows:

$$\theta \approx 483\ w^{1/2}\left(\frac{\overline{E}_m}{32 - t_0}\right)^{1/3} - 72 - 58\left(1 - \frac{1}{1.35^{\alpha_i}}\right),\ \text{deg} \qquad (1)$$

Thus, equation (1) relates the ice angle θ to the icing and operating conditions that are generally known or calculable in a flight performance study.

Ice height. - In a manner similar to that for the angle θ, the ice height h was correlated with the various icing conditions, as shown in figure 9. The relations shown in this figure yield the following expression:

$$h \approx 4.35\times10^{-4}\ \tau V_0 \sqrt{w\overline{\beta}_m}\ (32 - t_0)^{0.3},\ \text{in.} \qquad (2)$$

In equation (2) h varies approximately linearly with icing time and velocity. Figure 6 shows that the ice weight increased linearly with time for rime icing conditions but exceeded a linear relation for glaze icing conditions. These peculiarities may be explained by the geometry of the ice shape. Whereas rime icing deposits tend to grow directly into the airstream and thus form rectangular cross sections, glaze icing deposits grow both forward and laterally, and resemble triangular (or trapezoidal) cross sections with the base growing away from the airfoil. Thus, the area of a rectangle (analogous to weight of rime ice) increases linearly with its length (dimension h), while the area of a triangle (weight of glaze ice) increases faster than its height, by virtue of the increasing base. Therefore, the observed linear variation of ice height with time (fig. 9) is not inconsistent with the trends of ice weight against time (fig. 6).

The present measurements of airfoil ice formations were all obtained on the 6-foot-chord airfoil, and consequently body size (or chord) was not varied. However, the ice height correlation of equation (2) agrees remarkably well with unpublished measurements obtained on the following bodies: 0.8-inch-chord streamlined strut, 0.5-inch-diameter cylinder, and 0.1-inch-diameter cylinder. As noted in the preceding section, the ice-angle correlation also agreed with limited data obtained on a 1/2-inch-diameter cylinder. These unpublished data substantiate the correlations given for ice height and angle, which should be valid over a considerable range of body size and shape.

4438

Correlation Between Ice Shape and Drag-Coefficient Changes

Changes in airfoil drag coefficients due to protuberances are shown in reference 10 to vary linearly with protuberance height-to-chord ratio in most cases. As discussed previously, and in references 9 and 11, changes in airfoil drag coefficients due to ice formations are also expected to vary almost linearly with some ratio of ice thickness to chord (herein h/c). Consequently, a linear relation was assumed for simplicity, and the change in drag coefficient due to ice (ΔC_D) was divided by the height-to-chord ratio h/c to remove the ice thickness variation from the drag change and permit a study of the other variables. In figure 10 the term $\Delta C_D c/100h$ is plotted against the angle θ for the airfoil data in table II. The ordinate is the change in drag coefficient caused by the various ice formations corrected to a common height equal to 1 percent of chord. These drag-coefficient changes are shown for each angle of attack investigated.

Data scatter in figure 10 is again considerable, but mean curves for each angle-of-attack condition are readily discernible. The trends with respect to θ and α are very pronounced. As discussed in reference 2, the airfoil drag coefficient is considerably reduced by the addition of ice at the higher angles of attack and negative angles of θ. For figure 10, the relations given in equations (1) and (2) were utilized to determine θ and h, respectively. Thus, as shown by the scale legends, the terms θ and h, which generally are unknown, are eliminated and ΔC_D may be determined from known icing and operating conditions.

The tailed symbols in figure 10 represent cases in which ice was formed at an angle of attack α_i and the airfoil was then changed to an angle α, for which C_D was measured and ΔC_D was obtained from the clean-airfoil drag coefficient at the angle α. These data aline themselves very well with the balance of the data taken at fixed angles of attack and thus serve to corroborate the usefulness of θ in correlating ΔC_D for this airfoil. Because of this, figure 10 may also be used to assess the drag-coefficient changes at many angles of attack due to an ice deposit formed at a particular angle of attack.

4438

CC-2 back

Final Correlation Between Drag-Coefficient Changes and Icing Conditions

By use of figure 10 the changes in airfoil-section drag coefficients due to ice formations may be determined from the icing and operating conditions. These relations are shown for each of several angles of attack. To obtain a complete relation, it is necessary to determine an equation to account for the effects of angle of attack in figure 10. A trigonometric equation form was selected to fit the curves in figure 10 for two reasons. First, the data fitted into curves suggestive of sine functions somewhat better than into straight lines; and second, reasoning as to the probable nature of the curves beyond the data limits indicated that each curve would probably have a maximum and a minimum value as a function of θ. The resulting expression is as follows:

$$\Delta C_D \approx \left[8.7\times10^{-5}\,\frac{\tau V_0}{c}\sqrt{w\bar{\beta}_m}(32-t_0)^{0.3}\right]\left[1 + 6\left\{(1 + 2\sin^4 12\alpha)\sin^2\left[543\sqrt{w}\sqrt[3]{\frac{\bar{E}_m}{32-t_0}} - 81 + 65.3\left(\frac{1}{1.35^{\alpha_i}} - \frac{1}{1.35^{\alpha}}\right)\right] - 1.7\sin^4 11\alpha\right\}\right] \tag{3}$$

The first bracket of equation (3) accounts for the height-to-chord ratio of the ice that acts as a flow spoiler, and the second bracket accounts for the ice angle, the angle of attack, and the case wherein ice is formed at an angle of attack different from that under consideration. This latter case is accounted for by the term $65.3\left(\frac{1}{1.35^{\alpha_i}} - \frac{1}{1.35^{\alpha}}\right)$, which vanishes when ice is formed at the same angle of attack as that being considered $(\alpha_i = \alpha)$. In the $\sin^2$ function in the second bracket of equation (3) the expression $543\sqrt{w}\sqrt[3]{\frac{\bar{E}_m}{32-t_0}} - 81$ is valid between the limits of 0 and 180; beyond these limits a value of zero should be used for the expression instead of a calculated number.

The measured ΔC_D values from table II are plotted in figure 11 against the calculated values using equation (3). The mean value of the data points falls on the line of perfect agreement, and the standard deviation from the mean is ± 0.0059, which indicates that about 68 percent of the calculated data points agree with the measured values within a ΔC_D difference of 0.0059.

CONCLUDING REMARKS

It should be noted that the preceding correlation is a first-order approximation applicable to an unswept NACA 65A004 airfoil section, and extension of the variables beyond the range of present data might give erroneous results. The present analysis shows primarily that correlations between icing conditions, icing deposits, and aerodynamic drag characteristics are possible. For a correlation of similar data for a variety of airfoils, the present equation would need additional variables to account for airfoil shape.

The present data correlation is influenced greatly by the thinness of the airfoil, the pointed leading edge, and the flow separation from the upper surface at high angles of attack. Thicker airfoils with blunt leading edges would have few or no cases of drag reductions with ice, and any correlation among ice shape, angle of attack, and change in drag would probably be more orderly.

The drag-coefficient changes due to ice formations are predicted by the final equation virtually without limits (e.g., with very long icing times). Realistically, however, drag increases are eventually limited by presently unknown shedding characteristics of the ice, and drag reductions are probably limited to values that yield section drag coefficients comparable to those of the lowest-drag airfoil sections known at the particular angle-of-attack condition.

This correlation concerns only the changes in section drag coefficients; changes in lift and pitching-moment coefficients were not studied; however, estimates of the lift and pitching-moment changes can be made based on the trends in the aerodynamic data of NACA TN 4155. Also, a similar analysis for lift and moment coefficient changes could probably be made from the data of TN 4155.

Several secondary factors were ignored in making the present analysis. In reducing the ice shape to two dimensions, an angle and a height, the following factors were unaccounted for: relative bluntness or sharpness of the peak of the ice formation, chordwise location of the upper-surface edge of the ice formation, and amount and location of lower-surface ice. These factors all have noticeable effects on the aerodynamic data and would undoubtedly reduce the data scatter if properly accounted for. However, this correlation should be useful in estimating the effects of icing encounters on various flight operations and missions. For these estimates, direct and internally consistent calculations can be made with the final equation derived in this report.

SUMMARY OF RESULTS

From an analysis of impingement, ice deposits, and aerodynamic drag for an unswept NACA 65A004 airfoil section exposed to icing conditions

in the NACA Lewis icing tunnel, the following principal results were obtained:

1. A general correlation was obtained relating the change in airfoil-section drag coefficient due to ice formations to the following icing and operating conditions: icing time, airspeed, chord length, liquid-water content, cloud droplet impingement efficiencies, air total temperature, and airfoil angles of attack.

4438

2. It was found possible to relate changes in airfoil drag coefficients to two significant measurements of the ice formations, a height dimension and an ice angle.

3. A variety of ice formations were photographed, weighed, cross-sectioned, measured, and correlated with the icing conditions in which they were formed.

4. Ice-formation weights increased at approximately constant rates with increasing time in a rime icing condition and at progressively increasing rates in glaze icing conditions. Initial rates of ice collection agreed reasonably well with values predicted from droplet impingement data.

5. Experimental droplet impingement rates on this airfoil section agreed with previous theoretical calculations for angles of attack of 4° or less. Disagreement at higher angles of attack was attributed to flow separation from the upper surface of the experimental airfoil model.

6. An equation is derived that can be used in conjunction with TN 4155 in estimating the effects of icing encounters on flight performance for an NACA 65A004 airfoil section.

Lewis Flight Propulsion Laboratory
National Advisory Committee for Aeronautics
Cleveland, Ohio, August 28, 1957

APPENDIX

SYMBOLS

C_D airfoil-section drag coefficient

$C_{D,0}$ clean-airfoil-section drag coefficient

ΔC_D change in section drag coefficient due to addition of ice

c airfoil chord length, in.

d volume-median droplet diameter, microns (3.94×10^{-5} in.)

$\overline{E}_m$ total droplet impingement efficiency, $\frac{c}{H}\int_{(s/c)_{l,lim}}^{(s/c)_{u,lim}} \overline{\beta}\, d(s/c)$, dimensionless

H frontal height of airfoil projected parallel to free-stream velocity direction, in.

h height of ice, in. (see eq. (2) and fig. 7)

K_0 modified inertia parameter, $\approx 1.87\times10^{-7}\left(\frac{V_0}{\mu}\right)^{0.6}\frac{d^{1.6}}{\rho^{0.4}c}$

s surface distance from zero-chord point, in.

t_0 free-stream total air temperature, °F

V_0 free-stream velocity, mph, or knots × 1.15

$\overline{W}_\beta$ local impingement rate, lb water/(hr)(sq ft)

$\overline{W}_m$ total water-impingement rate, $4.57\times10^{-4}\ V_0 w H \overline{E}_m$, lb/(min)(ft span)

w liquid-water content of cloud, g/cu m

α airfoil geometric angle of attack, deg

α_i airfoil geometric angle of attack at which ice deposit is formed, deg

$\overline{\beta}$ local droplet impingement efficiency, $\overline{W}_\beta/0.329\ V_0 w$, dimensionless

$\overline{\beta}_m$ maximum local droplet impingement efficiency, dimensionless

μ viscosity of air, lb mass/(ft)(sec)

ρ density of air, lb mass/cu ft

τ icing time, min

θ ice angle, deg (see eq. (1) and fig. 7)

Subscripts:

u upper surface

l lower surface

lim limit of impingement

Superscript:

$\bar{}$ value determined for experimental distribution of droplet sizes

REFERENCES

1. Dickey, Thomas A.: An Analysis of the Effects of Certain Variables in Determining the Form of an Ice Accretion. AEL 1206, Aero. Eng. Lab., Naval Air Exp. Station, May 29, 1952.

2. Gray, Vernon H., and von Glahn, Uwe H.: Aerodynamic Effects Caused by Icing of an Unswept NACA 65A004 Airfoil. NACA TN 4155, 1957.

3. von Glahn, Uwe H., Gelder, Thomas F., and Smyers, William H., Jr.: A Dye-Tracer Technique for Experimentally Obtaining Impingement Characteristics of Arbitrary Bodies and a Method for Determining Droplet Size Distribution. NACA TN 3338, 1955.

4. Gelder, Thomas F., Smyers, William H., and von Glahn, Uwe: Experimental Droplet Impingement on Several Two-Dimensional Airfoils with Thickness Ratios of 6 to 16 Percent. NACA TN 3839, 1956.

5. Brun, Rinaldo J., and Vogt, Dorothea E.: Impingement of Water Droplets on NACA 65A004 Airfoil at 0° Angle of Attack. NACA TN 3586, 1955.

6. Brun, Rinaldo J., Gallagher, Helen M., and Vogt, Dorothea E.: Impingement of Water Droplets on NACA 65A004 Airfoil and Effect of Change in Airfoil Thickness from 12 to 4 Percent at 4° Angle of Attack. NACA TN 3047, 1953.

7. Brun, Rinaldo J., Gallagher, Helen M., and Vogt, Dorothea E.: Impingement of Water Droplets on NACA 65A004 Airfoil at 8° Angle of Attack. NACA TN 3155, 1954.

8. von Glahn, Uwe H.: Use of Truncated Flapped Airfoils for Impingement and Icing Tests of Full-Scale Leading-Edge Sections. NACA RM E56E11, 1956.

9. Gray, Vernon H., and von Glahn, Uwe H.: Effect of Ice and Frost Formations on Drag of NACA 65_1-212 Airfoil for Various Modes of Thermal Ice Protection. NACA TN 2962, 1953.

10. Jacobs, Eastman N.: Airfoil Section Characteristics as Affected by Protuberances. NACA Rep. 446, 1932.

11. Bowden, Dean T.: Effect of Pneumatic De-Icers and Ice Formations on Aerodynamic Characteristics of an Airfoil. NACA TN 3564, 1956.

4438

TABLE I. - FRONTAL HEIGHT OF NACA 65A004 AIRFOIL

Geometric angle of attack, α, deg	Ratio of frontal height to chord, H/c
0	0.040
2	.0465
4	.0756
6	.1085
8	.1425
10	.177
12	.211

CC$_4$-3

TABLE II. - ICING AND AERODYNAMIC

Angle of attack, α, deg	Angle of attack during icing, α_i, deg	Airspeed, V_0, mph	Air total temperature, t_0, °F	Liquid-water content, w, $\frac{g}{cu\ m}$	Volume-medium droplet diameter, d, microns	Airfoil impingement efficiency, $\bar{E}_m$	Maximum local impingement efficiency, $\bar{\beta}_m$	Leading-edge ice angle, θ, deg	Leading-edge ice height, h, in.
0	0	175	10	1.86	19.0	0.124	0.744	53	0.63
								48	1.25
								51	2.0
			25	1.45	16.5	0.118	0.742	--	0.42
								--	1.0
								--	1.50
			10	0.95	13.7	0.100	0.739	5	1.38
				1.45	16.5	0.119	0.742	40	1.38
		275	10	0.90	15.0	0.127	0.744	21	1.5
			25	1.20	17.5	0.145	0.761	50	2.0
				0.63	12.5	0.11	0.741	38	2.0
				0.90	15.0	0.11	0.761	50	1.38

4438

DATA FOR NACA 65A004 AIRFOIL

Icing time, τ, min	Weight of ice collected, lb/ft span	Theoretical impingement, lb/ft span	Clean-airfoil drag coefficient, $C_{D,0}$	Change in airfoil drag coefficient due to ice, ΔC_D	Ice cross section on 1/4-inch grid	Comments
3	0.225	0.159	0.0062	0.0092	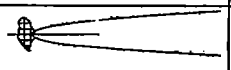	
6	0.48	0.319	0.0062	0.0204	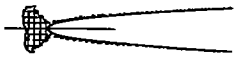	
10	1.14	0.531	0.0062	0.0307	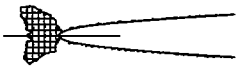	
3	0.12	0.118	0.0062	------	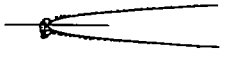	Possible variations in test conditions
7	0.34	0.276	0.0062	------	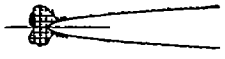	Possible variations in test conditions
12	0.69	0.473	0.0062	------	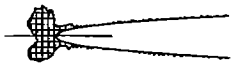	Possible variations in test conditions
10	0.27	0.219	0.0062	0.0069	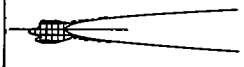	Partial ice shedding
9	-----	0.355	0.0062	0.0199	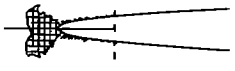	
7	0.39	0.262	0.0062	0.0100	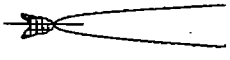	
12	-----	0.755	0.0062	0.0380	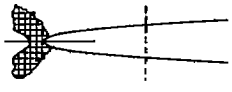	
14.4	-----	0.361	0.0062	0.0306	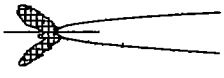	
9	-----	0.323	0.0062	0.0256	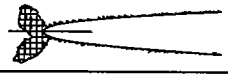	

4438

CC-3 back

TABLE II. - Continued. ICING AND AERO-

Angle of attack, α, deg	Angle of attack during icing, α_i, deg	Air-speed, V_0, mph	Air total temperature, t_0, °F	Liquid-water content, w, $\frac{g}{cu\ m}$	Volume-medium droplet diameter, d, microns	Airfoil impingement efficiency, $\bar{E}_m$	Maximum local impingement efficiency, $\bar{\beta}_m$	Leading-edge ice angle, θ, deg	Leading-edge ice height, h, in.
0	0	275	0	0.90	15.0	0.127	0.744	2	2.0
2	2	175	0	1.45	16.5	0.158	0.667	-14	1.30
								-13	2.38
				0.95	13.7	0.126	0.66	-11	1.88
			10	0.95	13.7	0.126	0.66	-13	1.75
				1.86	19.0	0.168	0.665	18	1.13
				1.45	16.5	0.158	0.665	20	2.0
			25	1.45	16.5	0.160	0.665	---	0.38
								---	0.75
								43	1.5
								52	1.65

4438

4438

DYNAMIC DATA FOR NACA 65A004 AIRFOIL

Icing time, τ, min	Weight of ice collected, lb/ft span	Theoretical impingement, lb/ft span	Clean-airfoil drag coefficient, $C_{D,0}$	Change in airfoil drag coefficient due to ice, ΔC_D	Ice cross section on 1/4-inch grid	Comments
7	0.39	0.29	0.0062	------	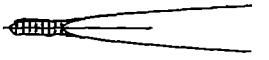	
5	0.405	0.307	0.0066	0.0073	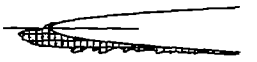	
10	0.810	0.613	0.0066	0.0109	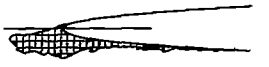	
12	0.585	0.385	0.0066	0.0091	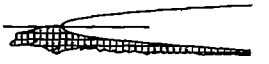	
12.25	0.39	0.393	0.0066	0.0078	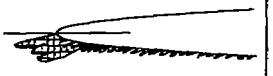	
5.75	-----	0.481	0.0066	0.0181	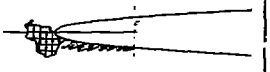	
9.17	-----	0.563	0.0066	0.0231	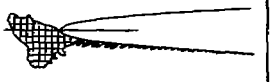	
3	0.195	0.186	0.0066	0.0091		
7	0.48	0.435	0.0066	0.0162	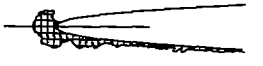	
14	1.04	0.86	0.0066	0.0303		Partial ice shedding
13	-----	0.807	0.0066	0.0265		

TABLE II. - Continued. ICING AND AERO-

Angle of attack, α, deg	Angle of attack during icing, α_i, deg	Airspeed, V_0, mph	Air total temperature, t_0, °F	Liquid-water content, w, $\frac{g}{cu\ m}$	Volume-medium droplet diameter, d, microns	Airfoil impingement efficiency, $\bar{E}_m$	Maximum local impingement efficiency, $\bar{\beta}_m$	Leading-edge ice angle, θ, deg	Leading-edge ice height, h, in.
2	2	275	0	0.90	15.0	0.177	0.668	-5	1.75
			25	0.90	15.0	0.145	0.663	---	0.56
								46	1.38
								45	1.75
								[a]51	2.0
			0	0.90	15.0	0.177	-----	-18	1.38
			10	0.90	15.0	0.176	-----	4	1.25
4	4	175	10	0.95	13.7	0.108	0.628	-22	2.13
				1.45	16.5	0.145	0.631	0	2.13
				1.86	19.0	0.157	0.636	21	1.5

[a]Estimated.

4438

4438

DYNAMIC DATA FOR NACA 65A004 AIRFOIL

Icing time, τ, min	Weight of ice collected, lb/ft span	Theoretical impingement, lb/ft span	Clean-airfoil drag coefficient, $C_{D,0}$	Change in airfoil drag coefficient due to ice, ΔC_D	Ice cross section on 1/4-inch grid	Comments
7	0.555	0.469	0.0066	0.0061	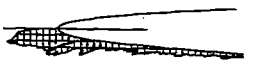	
3	0.165	0.164	0.0066	0.0109	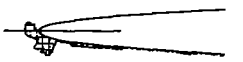	
8	0.60	0.438	0.0066	0.0244	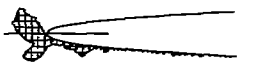	
12	0.60	0.657	0.0066	0.0370	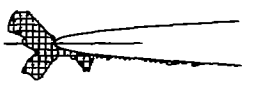	
9	-----	0.495	0.0066	0.0250	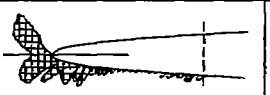	
--	-----	-----	0.0066	0.0057		Ice shedding
--	-----	-----	0.0066	0.0116	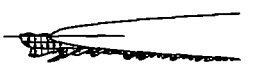	Ice shedding
13	-----	0.581	0.0197	-0.0030	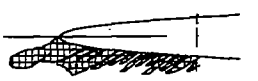	
10	-----	0.915	0.0197	0.0210	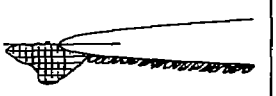	
8	1.14	1.015	0.0197	0.0277	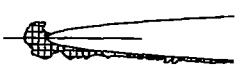	

TABLE II. - Continued. ICING AND AERO-

Angle of attack, α, deg	Angle of attack during icing, α_i, deg	Airspeed, V_0, mph	Air total temperature, t_0, °F	Liquid-water content, w, $\frac{g}{cu\ m}$	Volume-medium droplet diameter, d, microns	Airfoil impingement efficiency, $\bar{E}_m$	Maximum local impingement efficiency, $\bar{\beta}_m$	Leading-edge ice angle, θ, deg	Leading-edge ice height, h, in.
4	4	175	25	0.95	13.7	0.108	0.628	20	1.13
				1.45	16.5	0.148	0.636	---	0.53
								---	1.38
		275	0	0.45	11.3	0.108	0.628	-35	2.25
				0.90	15.0	0.165	0.637	-34	2.63
			10	0.63	12.5	0.128	0.63	-34	2.0
				0.90	15.0	0.165	0.637	-28	2.0
			25	0.90	15.0	0.128	0.63	35	2.00
				1.20	17.5	0.207	0.64	33	1.5
			10	1.20	17.5	0.200	0.64	-1	2.13
		175	25	1.45	16.5	0.148	0.637	13	0.88

4438

CC-4

DYNAMIC DATA FOR NACA 65A004 AIRFOIL

Icing time, τ, min	Weight of ice collected, lb/ft span	Theoretical impingement, lb/ft span	Clean-airfoil drag coefficient, $C_{D,0}$	Change in airfoil drag coefficient due to ice, ΔC_D	Ice cross section on 1/4-inch grid	Comments
10.33	0.42	0.457	0.0197	0.0195	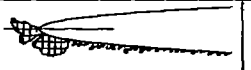	
3	0.225	0.279	0.0197	------	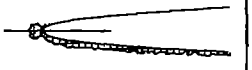	
12	0.885	1.12	0.0197	------	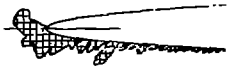	
17.67	-----	0.586	0.0197	-0.0059	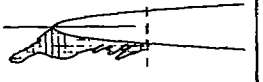	
8.33	-----	0.850	0.0197	-0.0040		
13.67	-----	0.753	0.0197	-0.0056	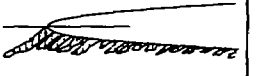	
10.75	-----	1.10	0.0197	0.0083	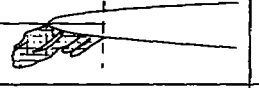	
11.25	-----	0.885	0.0197	0.0420	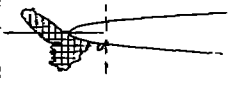	
7	-----	1.19	0.0197	0.0333		
7.5	-----	0.985	0.0197	0.0178	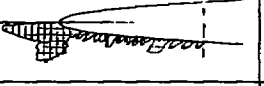	
6	0.445	0.560	0.0197	0.0157	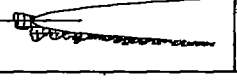	Possible variations in test conditions

TABLE II. - Continued. ICING AND AERO-

Angle of attack, α, deg	Angle of attack during icing, α_i, deg	Air-speed, V_0, mph	Air total temperature, t_0, °F	Liquid-water content, w, $\frac{g}{cu\ m}$	Volume-medium droplet diameter, d, microns	Airfoil impingement efficiency, $\bar{E}_m$	Maximum local impingement efficiency, $\bar{\beta}_m$	Leading-edge ice angle, θ, deg	Leading-edge ice height, h, in.
6	6	175	10	1.45	16.5	[a]0.12	[a]0.582	-19	2.0
				1.86	19.0	[a]0.13	[a]0.585	3	2.13
				0.95	13.7	[a]0.09	[a]0.578	-46	2.0
			25	1.45	16.5	[a]0.118	[a]0.583	27	1.25
8	8	175	10	1.86	19.0	[a]0.125	[a]0.517	1	1.5
				0.95	13.7	[a]0.08	[a]0.509	-47	2.25
				1.45	16.5	0.09	0.515	-40	2.0
			0	1.45	16.5	0.09	0.515	-52	1.25
									1.75
			25	1.45	16.5	0.09	0.515	15	0.88

[a]Estimated.

4438

4438

CC-4 back

DYNAMIC DATA FOR NACA 65A004 AIRFOIL

Icing time, τ, min	Weight of ice collected, lb/ft span	Theoretical impingement, lb/ft span	Clean-airfoil drag coefficient, $C_{D,0}$	Change in airfoil drag coefficient due to ice, ΔC_D	Ice cross section on 1/4-inch grid	Comments
10	-----	-----	0.0596	-0.0025	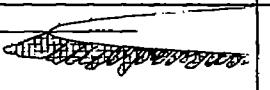	
10.5	-----	-----	0.0596	0.0280	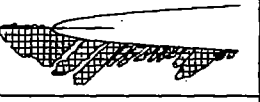	
13	-----	-----	0.0596	-0.0286	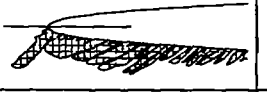	
10	0.90	1.04	0.0596	------	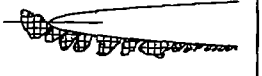	Possible ice shedding
8	-----	-----	0.119	0.0155	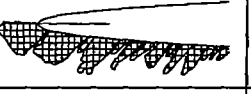	Possible ice shedding
12	-----	-----	0.119	-0.0450	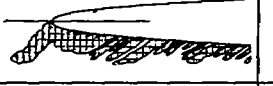	
11	-----	-----	0.119	-0.0300	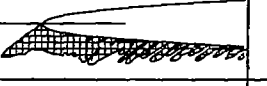	
7	0.841	0.751	0.119	------	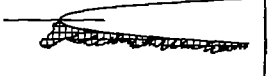	
-----	-----	-----	0.119	-0.0430	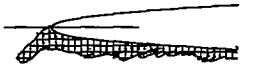	Poor spray condition
-----	-----	-----	0.119	0.0207	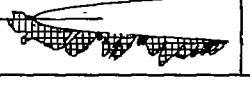	Ice shedding

TABLE II. - Concluded. ICING AND AERO-

Angle of attack, α, deg	Angle of attack during icing, α_i, deg	Airspeed, V_0, mph	Air total temperature, t_0, °F	Liquid-water content, w, $\frac{g}{cu\ m}$	Volume-medium droplet diameter, d, microns	Airfoil impingement efficiency, $\bar{E}_m$	Maximum local impingement efficiency, $\bar{\beta}_m$	Leading-edge ice angle, θ, deg	Leading-edge ice height, h, in.
10	10	125	10	2.0	18.0	[a]0.09	[a]0.54	-30	1.44
11	11	125	10	2.0	18.0	[a]0.09	[a]0.54	-34	1.75
				1.4	15.0	[a]0.08	[a]0.54	-49	1.63
4 6 8 10 11	2	175	10	0.95	13.7	0.126	0.66	-13	1.75
4 6 8 10 11	2	175	10	1.86	19.0	0.168	0.665	18	1.13
6 8 10 0 2	4	175	25	0.95	13.7	0.108	0.628	20	1.13
6 8 10 2	4	175	10	1.86	19.0	0.157	0.636	21	1.5

[a]Estimated.

4438

4438

DYNAMIC DATA FOR NACA 65A004 AIRFOIL

Icing time, τ, min	Weight of ice collected, lb/ft span	Theoretical impingement, lb/ft span	Clean-airfoil drag coefficient, $C_{D,0}$	Change in airfoil drag coefficient due to ice, ΔC_D	Ice cross section on 1/4-inch grid	Comments
10	-----	-----	0.187	-0.0020	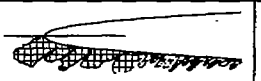	
11.5	-----	-----	0.214	-0.0105	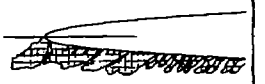	
10	-----	-----	0.214	-0.0280		
12.25	0.39	0.393	0.214	0.0005 -0.0049 -0.0160 -0.0080 0.006	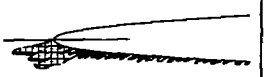	
5.75	-----	0.481	0.214	0.0208 0.0249 0.0273 0.0210 0.0160	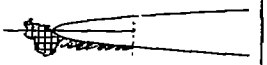	
10.33	0.42	0.457	0.214	0.0187 0.0170 0.0160 0.0097 0.0141	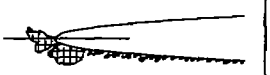	
8	1.14	1.015	0.214	0.0321 0.0330 0.0290 0.0238	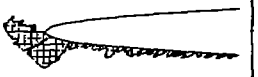	

4438

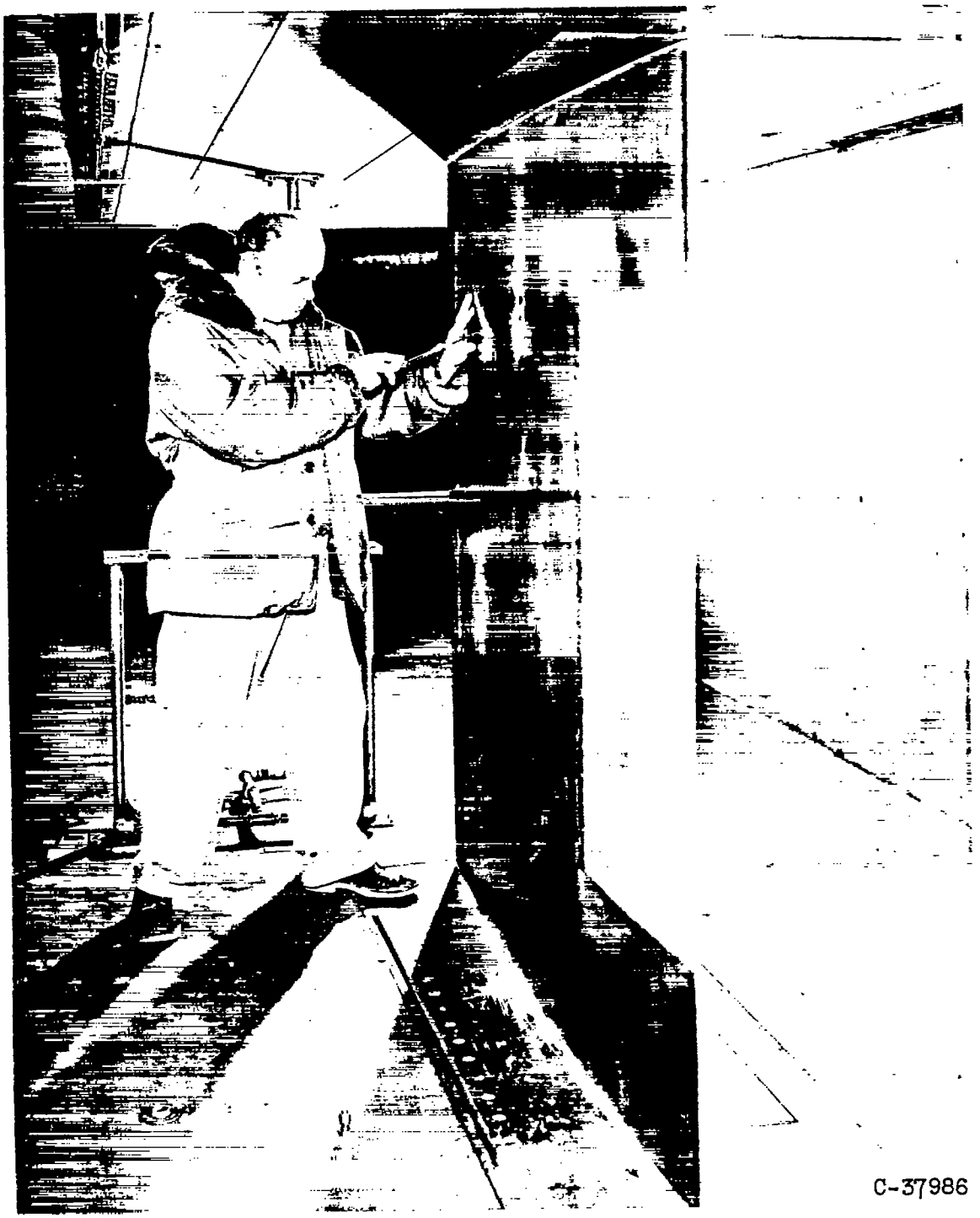

Figure 1. - Installation of NACA 65A004 airfoil in icing tunnel.

4438

(a) Celluloid sheet installed prior to icing exposure.

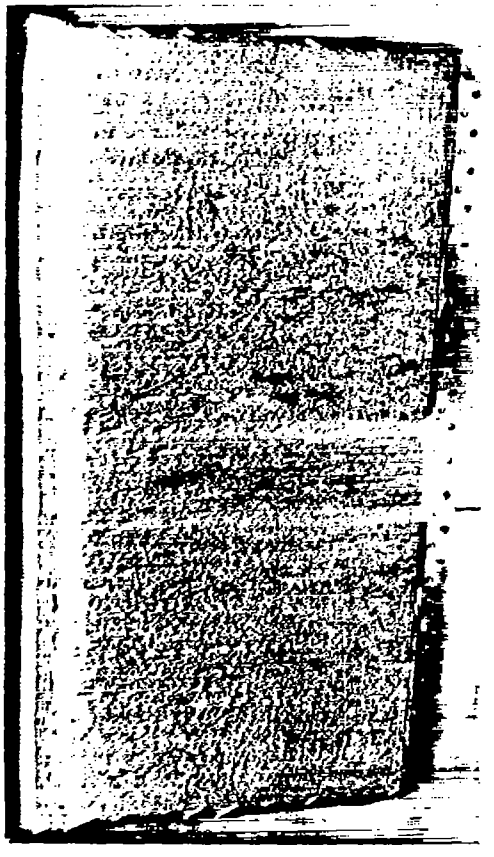

(b) Rime ice deposit on model and celluloid strip. Angle of attack, 2°.

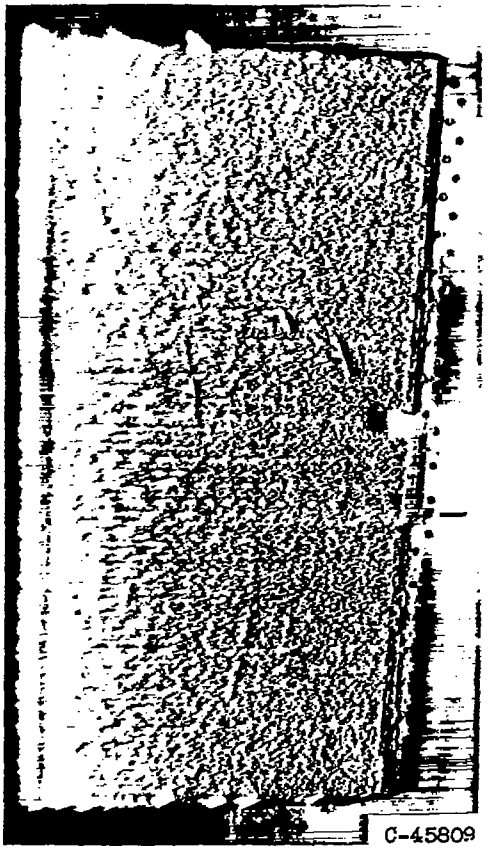

(c) Glaze-rime ice deposit on model and celluloid strip. Angle of attack, 8°.

Figure 2. - Airfoil at various stages in procedure of weighing and photographing ice formations.

4438

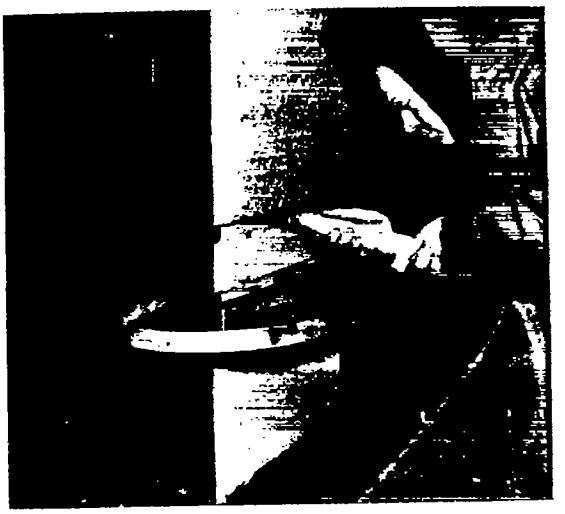

(d) Removal of ice with heated ice scraper prior to weighing.

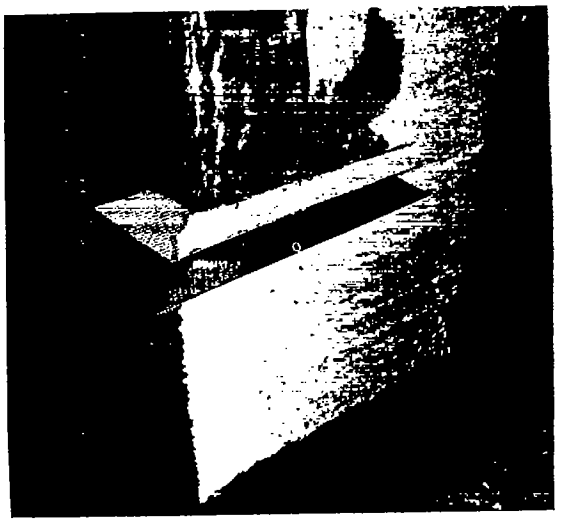

(e) Arrangement of wire grid and background prior to photographing.

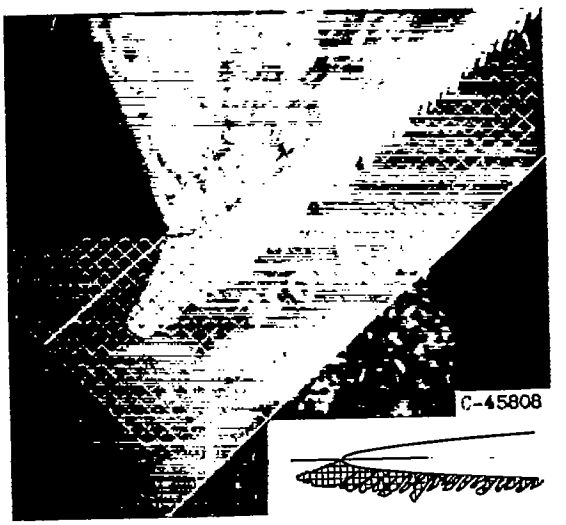

(f) Typical photograph of ice cross section with final two-dimensional sketch.

Figure 2. - Concluded. Airfoil at various stages in procedure of weighing and photographing ice formations.

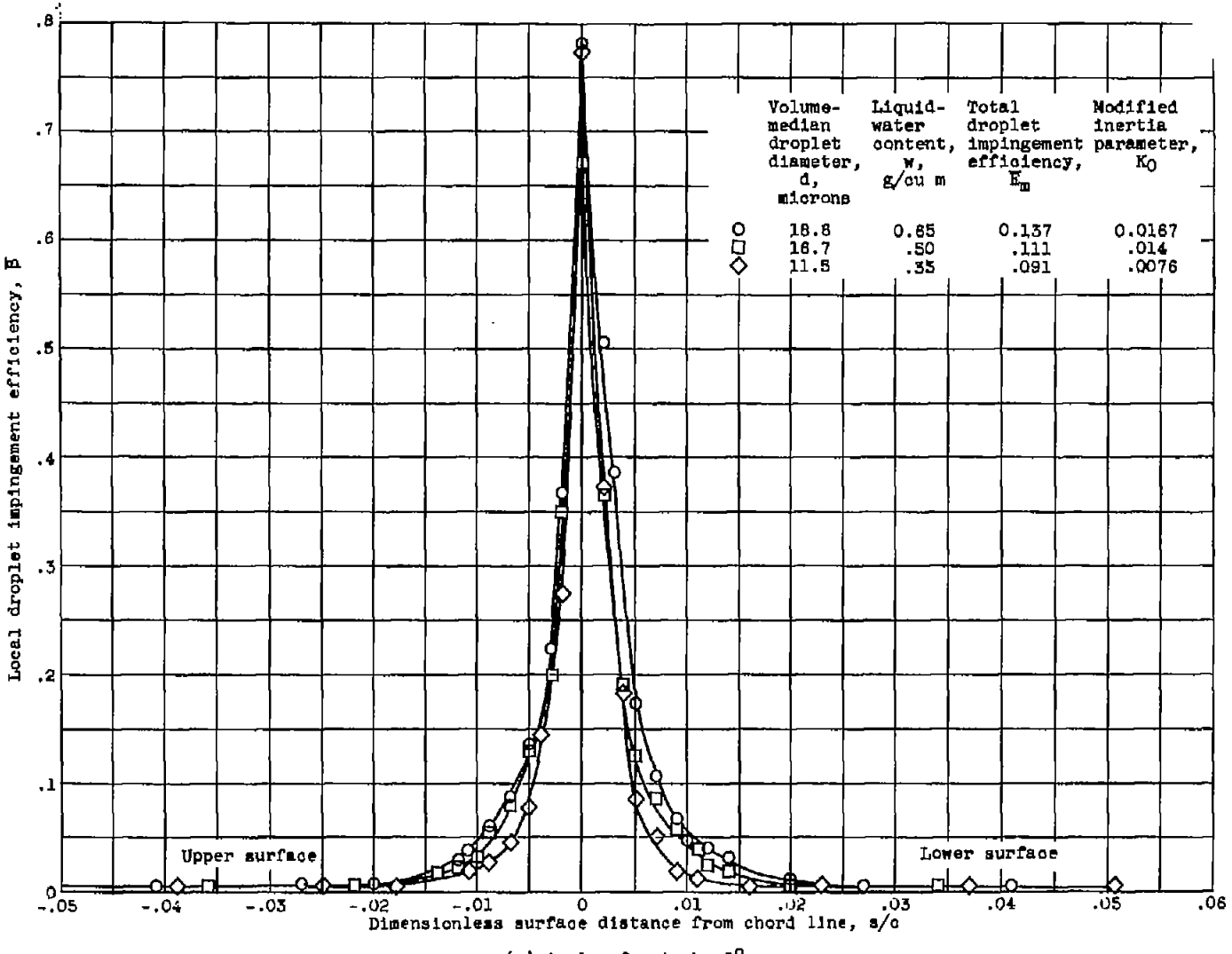

(a) Angle of attack, 0°.

Figure 3. - Chordwise variation of local droplet impingement efficiency for 6-foot-chord NACA 65A004 airfoil section.

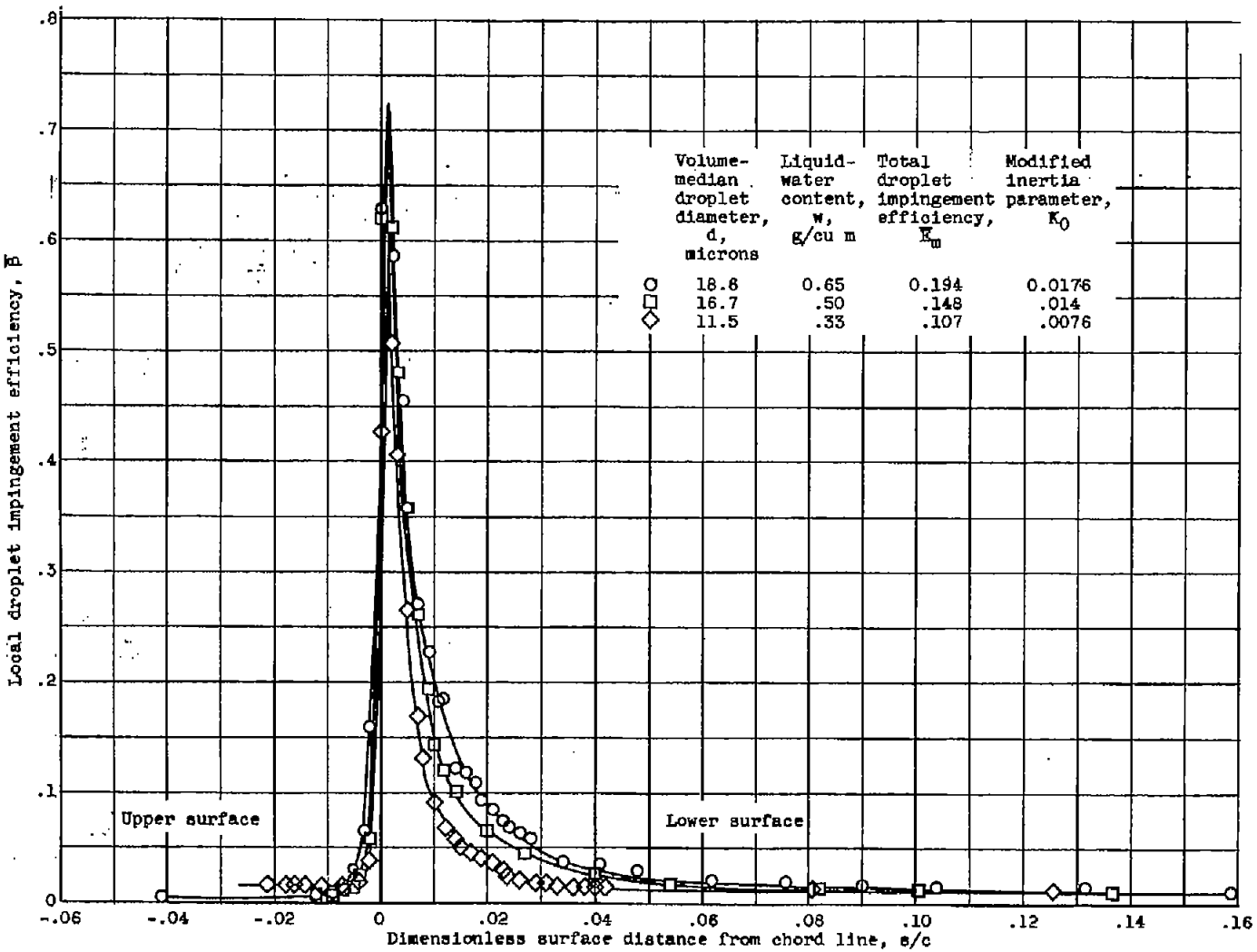

(b) Angle of attack, 2°.

Figure 3. - Continued. Chordwise variation of local droplet impingement efficiency for 6-foot-chord NACA 65A004 airfoil section.

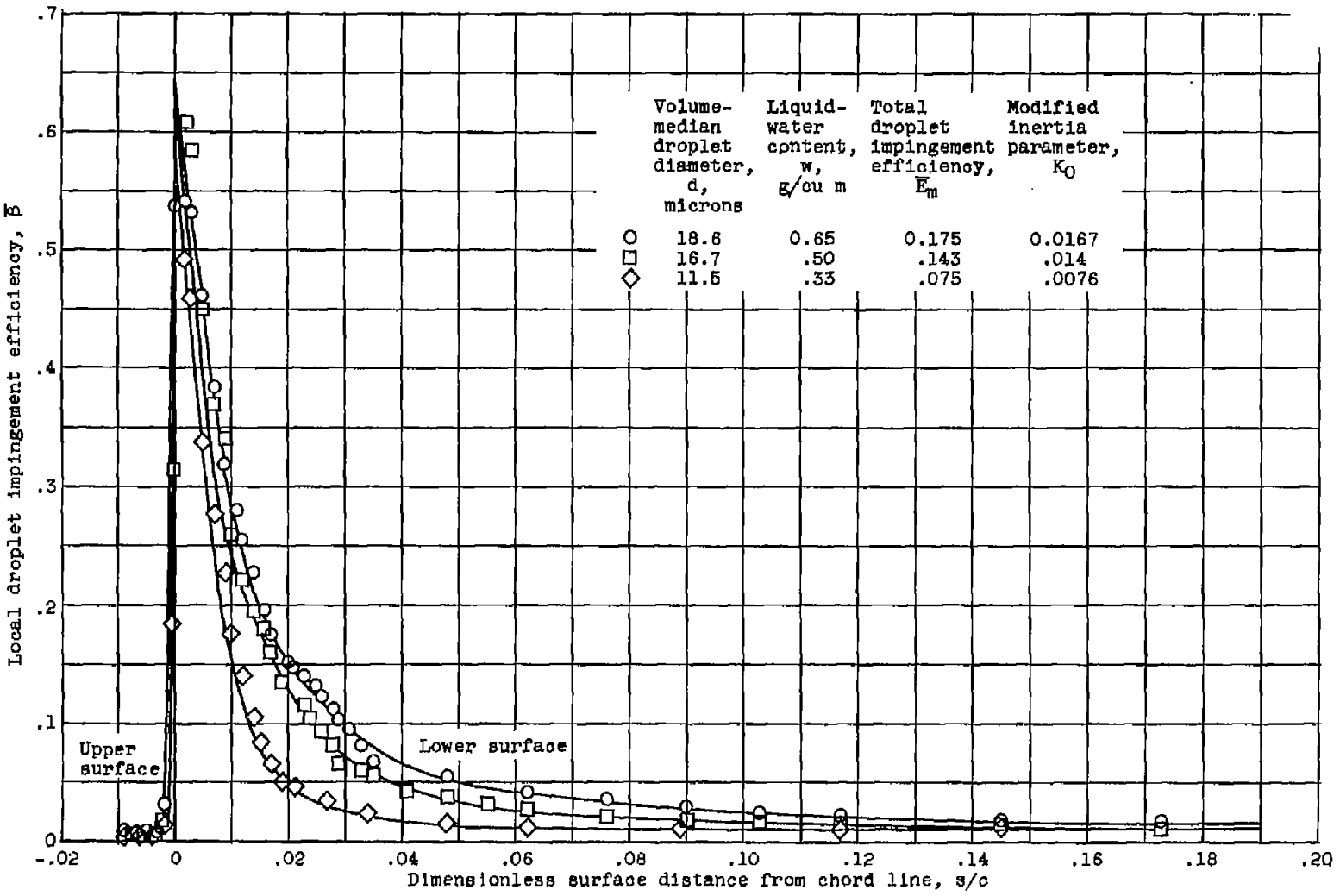

(c) Angle of attack, 4°.

Figure 3. - Continued. Chordwise variation of local droplet impingement efficiency for 6-foot-chord NACA 65A004 airfoil section.

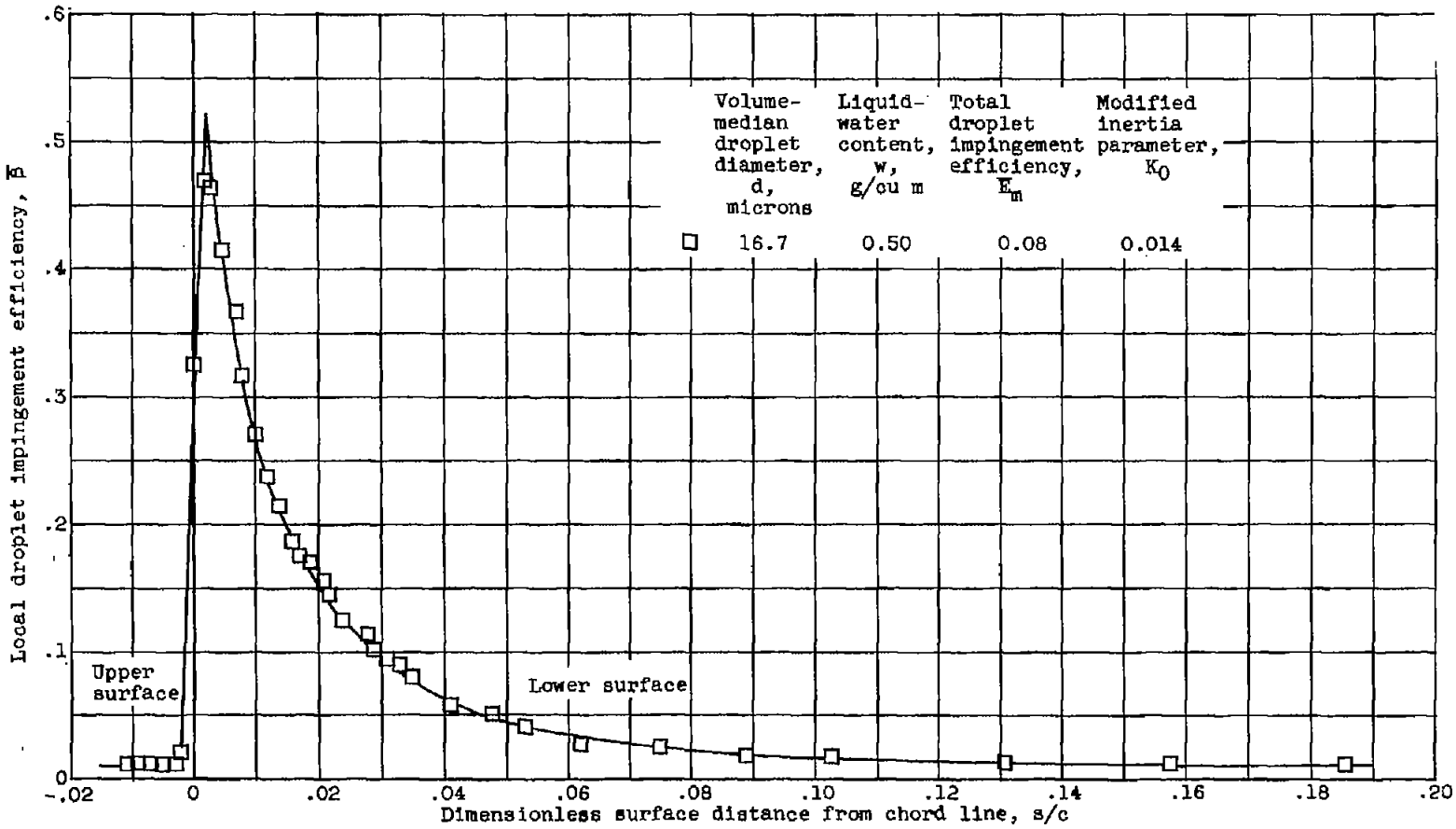

(d) Angle of attack, 8°.

Figure 3. - Concluded. Chordwise variation of local droplet impingement efficiency for 6-foot-chord NACA 65A004 airfoil section.

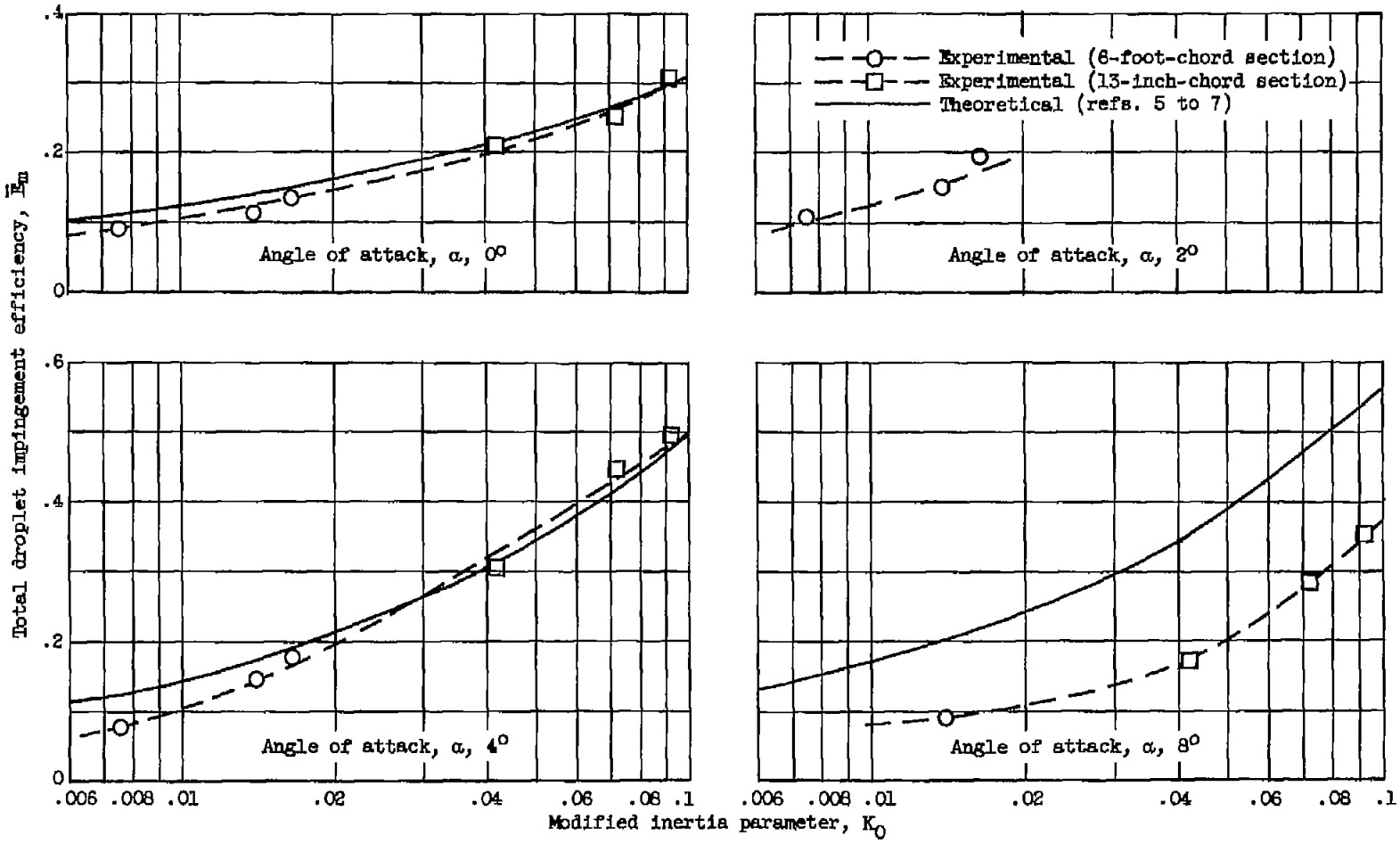

Figure 4. - Comparison of theoretical and experimental droplet impingement efficiency for NACA 65A004 airfoil on basis of modified inertia parameter.

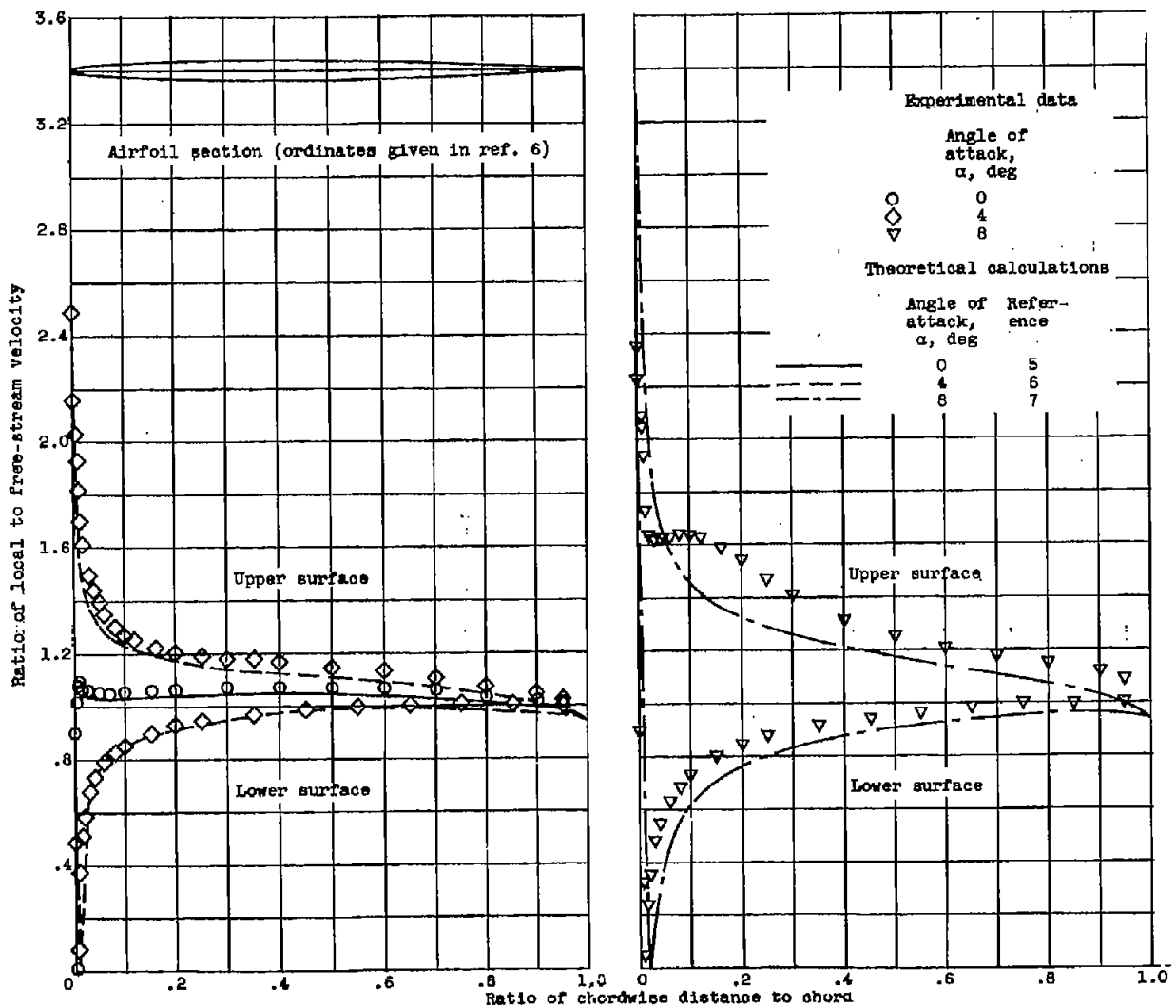

(a) Angles of attack, 0° and 4°.

(b) Angle of attack, 8°.

Figure 5. - Comparison of theoretical and experimental distribution of local velocity over 65A004 airfoil for three angles of attack.

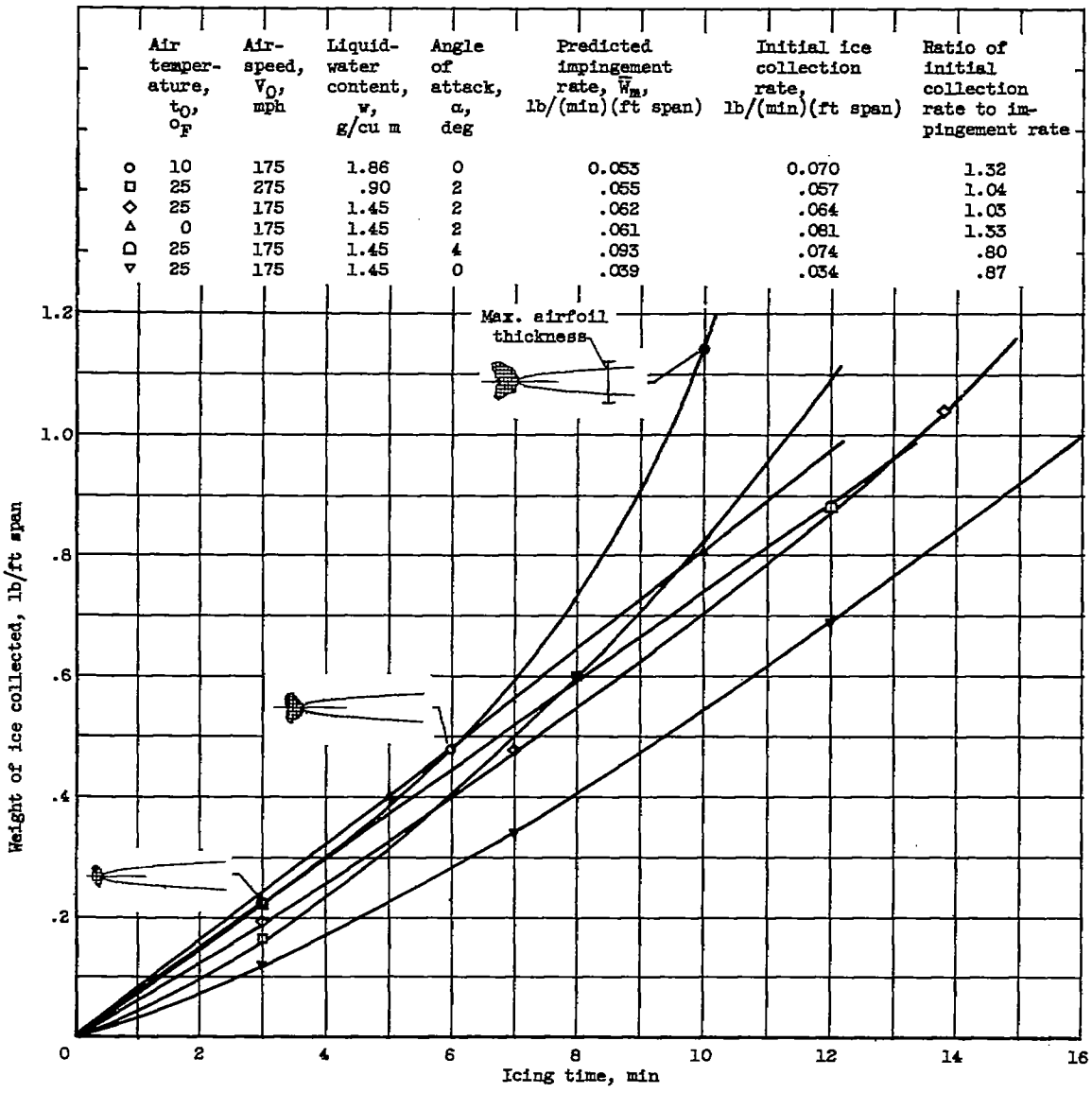

Figure 6. - Variation of ice collection rate with icing time and comparison with predicted impingement rate.

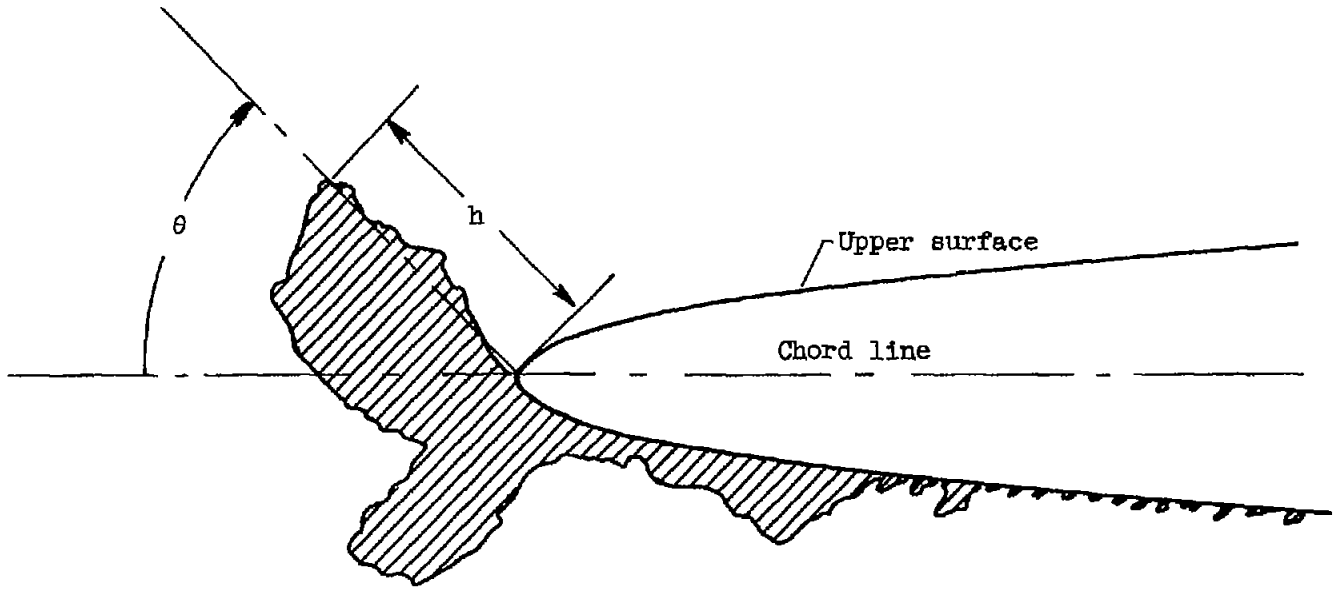

Figure 7. - Representation of ice shape by angle θ and height h.

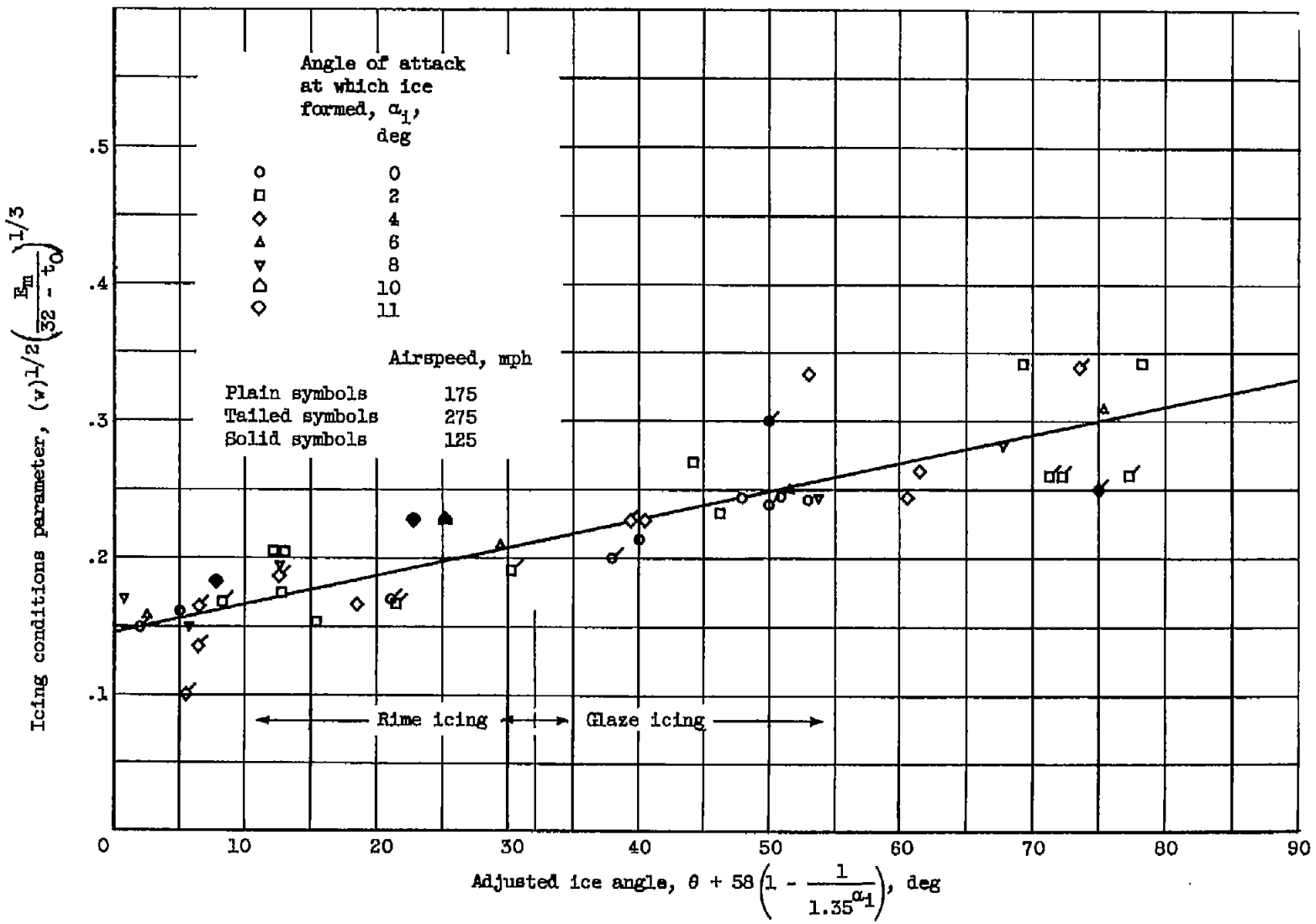

Figure 8. - Correlation of ice angle with icing conditions and angle of attack.

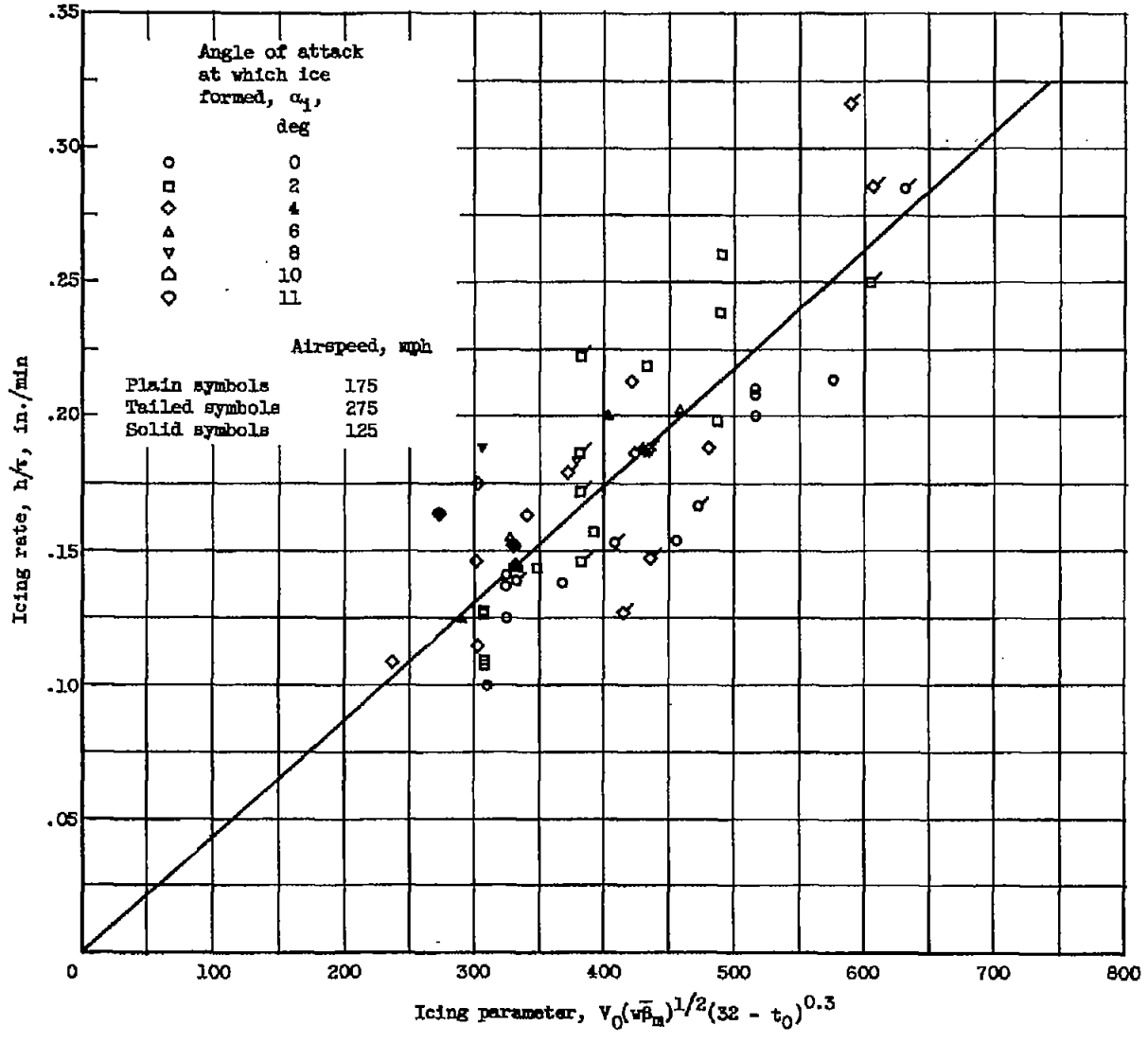

Figure 9. - Correlation of ice height with icing conditions.

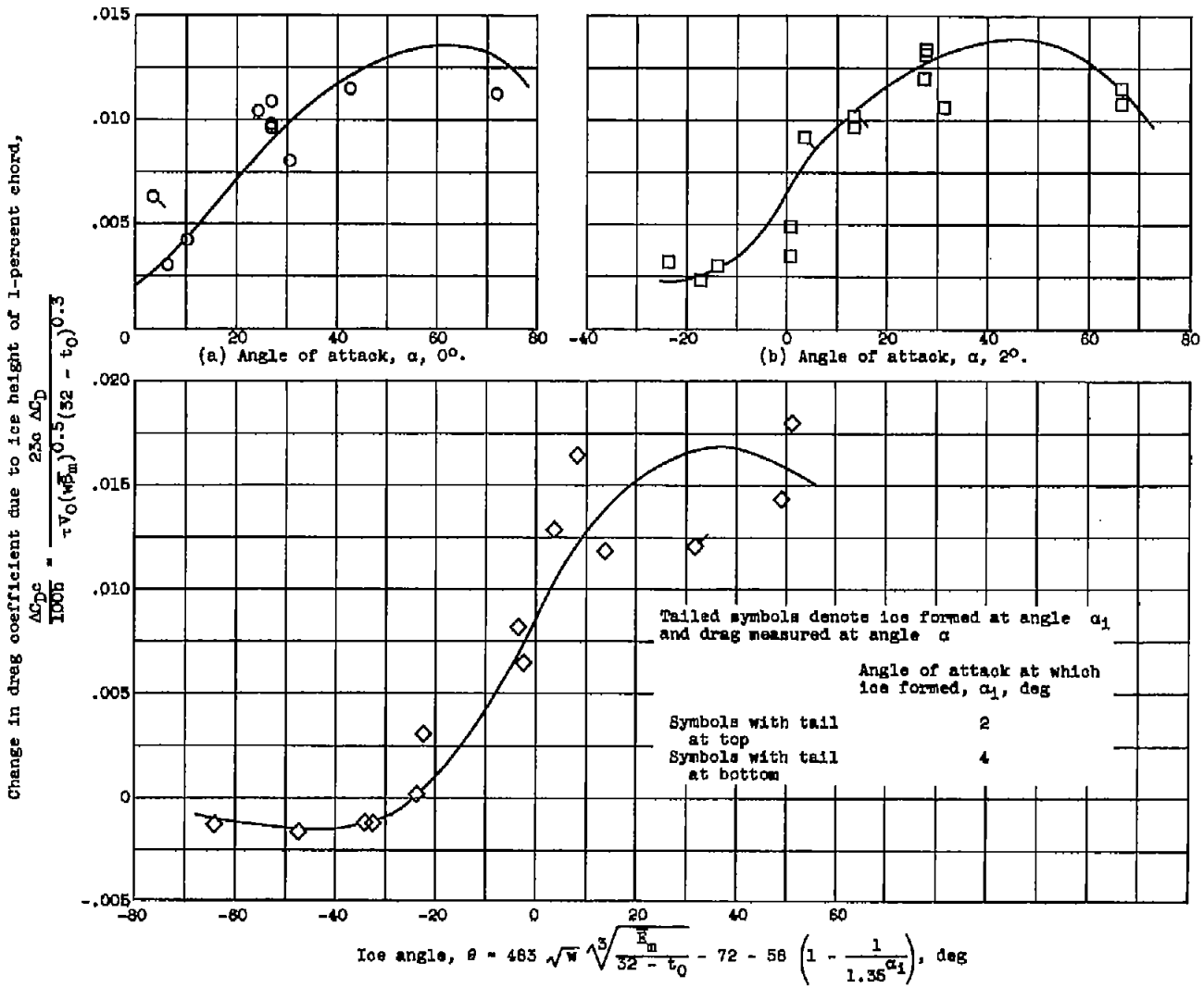

(c) Angle of attack, α, 4°.

Figure 10. - Change in airfoil drag coefficient due to ice height of 1-percent chord as function of ice angle and angles of attack.

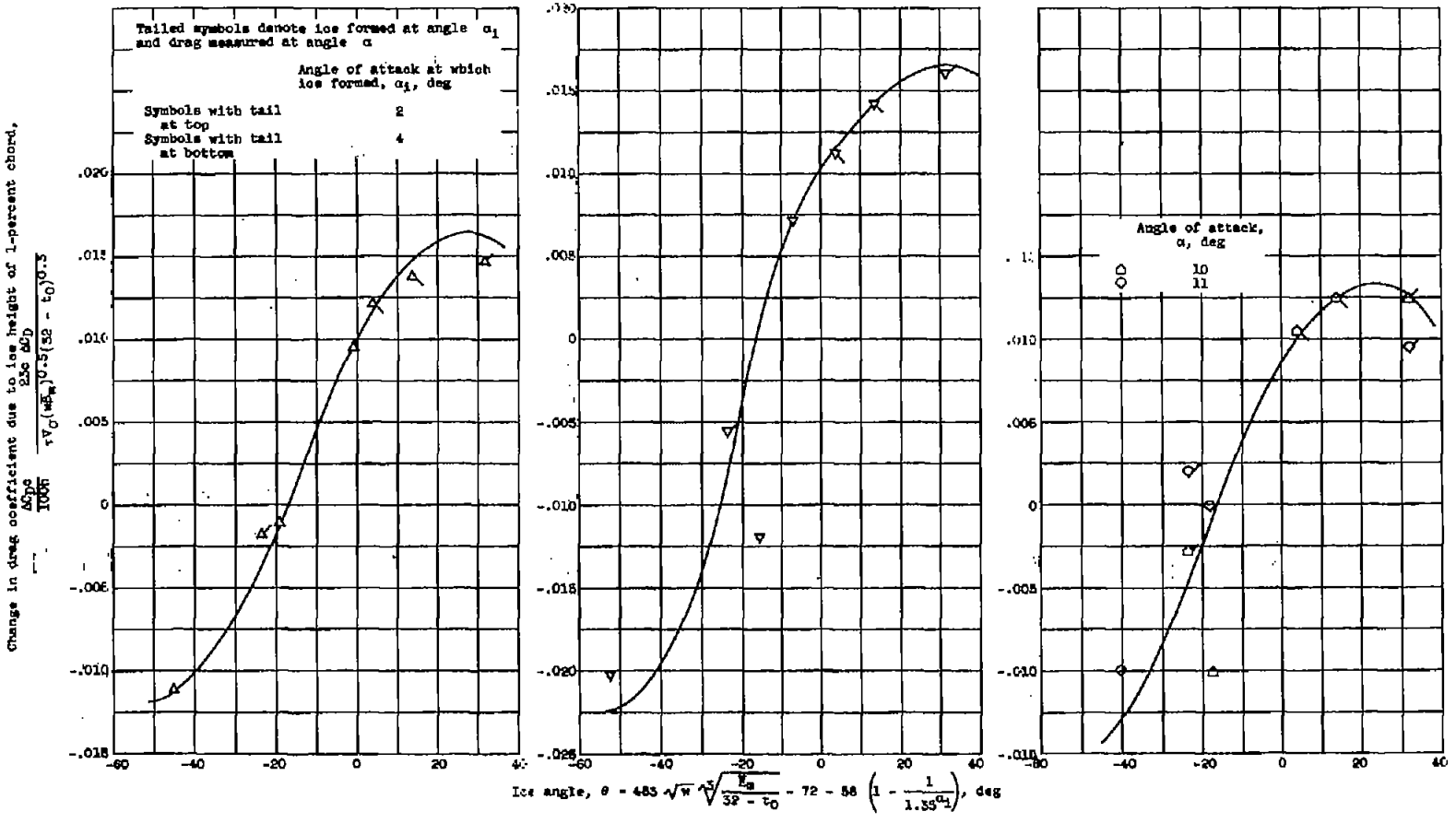

(d) Angle of attack, α, 6°. (e) Angle of attack, α, 8°. (f) Angles of attack, 10° and 11°.

Figure 10. - Concluded. Change in airfoil drag coefficient due to ice height of 1-percent chord as function of ice angle and angles of attack.

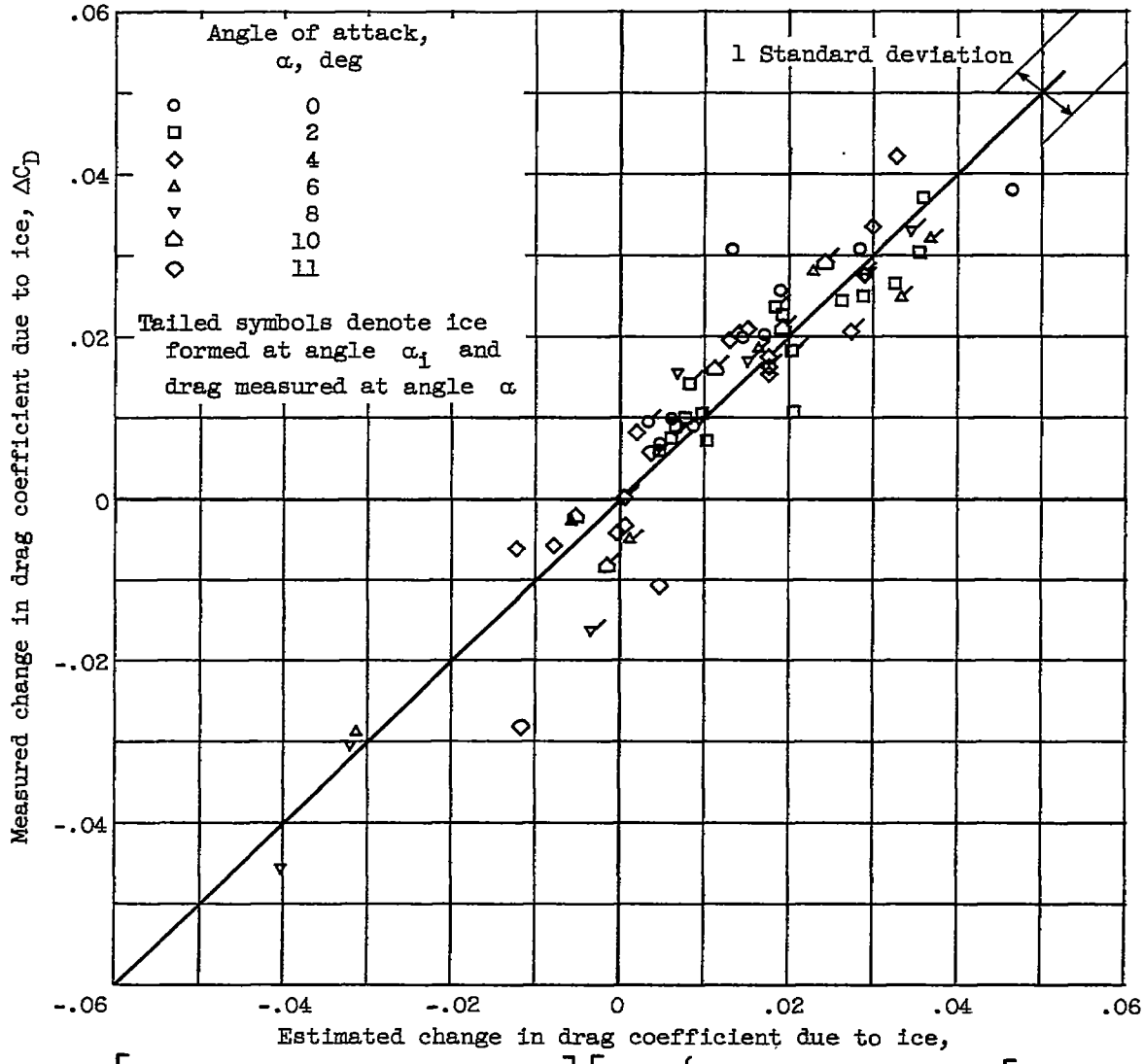

$$\left[8.7\times10^{-5}\,\frac{\tau V_0}{c}\sqrt{w\bar{\beta}_m}\,(32 - t_0)^{0.3}\right]\left[1 + 6\left\{(1 + 2\sin^4 12\alpha)\sin^2\left[543\sqrt{w}\sqrt[3]{\frac{\bar{E}_m}{32 - t_0}} - 81 + 65.3\left(\frac{1}{1.35^{\alpha_i}} - \frac{1}{1.35^{\alpha}}\right)\right] - 1.7\sin^4 11\alpha\right\}\right]$$

Figure 11. - Comparison of measured changes in drag coefficient due to ice formations with those calculated from empirically determined equation.